



OPTIMIZATION OF CAPILLARY ACTION & BRASS CONSUMPTION IN DIP-BRAZING OF ROADSTER BICYCLE FRAMES

Yoginder Nath Gupta^{1,*}, Arvind Kumar Singh², Surendra Singh³

¹Department of Mechanical Engineering - Ludhiana College of Engineering and Technology, Ludhiana- Chandigarh Highway, Katani Kalan, Ludhiana, Punjab, India – 141113.

²Hero Cycles Limited, Hero Nagar, GT Road, Ludhiana, Punjab, India-141003.

³Department of Metallurgical and Materials Engineering, Indian Institute of Technology, Roorkee-Haridwar Highway, Roorkee, Uttarakhand, India – 247667.

*corresponding author: e-mail: ynguptalacet@gmail.com; tel: 91 9501114747

Resume

This paper describes the requirements of joint clearance between the mating parts, of lugged bicycle frame head, to be brazed by flow of molten filler material (brass) between the micro gap due to capillary action. Tolerance analysis was done to establish the practical requirements of clearances essential to facilitate the assembly of the bicycle frame tubes and mating head lugs. Consumption of brass was computed, by weight measurements, after dip brazing of the lugged joints. Excessive joint clearance between the mating parts was reduced, by cold compaction of the assembled joint on mechanical power press using a press tool. The compacted joints were dip brazed by dipping it partially in the molten brass. Comparison of tensile strength of the brazed joints was done with respect to the strength of parent steel tubes. Brazed samples were sectioned to confirm the flow of brass all along the length of the lugs with improved capillary action. Thickness of the micro layer of the brass between the lug bore and tube outer surface was measured on optical microscope. Reduction in brass consumption due to reduced clearance was estimated volumetrically between the contact area between the lugs and the tubes.

Article info

Article history:

Received 20 May 2016

Accepted 31 October 2016

Online 31 January 2017

Keywords:

Dip brazing;
Capillary action;
Cold compaction;
Tensile strength;
Tolerance analysis.

Available online: <http://fstroj.uniza.sk/journal-mi/PDF/2016/17-2016.pdf>

ISSN 1335-0803 (print version)
ISSN 1338-6174 (online version)

1. Introduction

Dip brazing [1, 2] process is used in building the diamond shaped lugged frames of classic roadster bicycles [3, 4]. Lugged construction had been the primary method of assembling the roadster bicycle frames since early 20th century. Roadster frames are usually built from “Electric Resistance Welded” (ERW) [5, 6] CEW C1 type steel tubes push-fitted

inside the socket shaped sleeves, known as lugs. The lugs are primarily formed out of hot rolled carbon steel strips [7]. For brazing, every lugged joint is manually dipped in the molten brass maintained at a temperature slightly higher than its liquidus point 900 °C for brass with 60 % Copper and 40 % Zinc by weight [8] and chemical composition as shown in Table 1.

Table 1

Chemical Composition of Brass (wt. %).

	Tin	Lead	Zinc	Iron	Aluminum	Nickel	Silicon	Manganese	Phosphorus	Copper
Sample 1	0.041	0.012	36.590	0.036	0	0.005	0.000	0.004	0.012	63.100
Sample 2	0.039	0.016	37.950	0.013	0	0.000	0.020	0.074	0.020	61.150

Brazing takes place due to the flow of molten filler metal, between the surfaces of metals to be joined, by the principle of capillary action. As the filler metal (brass) cools down, it gets hardened thereby forming a joint connecting the tubes and the lugs. For the development of an effective capillary force [9] on molten filler metal or simply capillary action in brazing of metals, it is important to maintain a fairly uniform clearance between the mating surfaces of the joint. The tensile strength of the brazed joint decreases when the clearance between the joint is increased. Ideally there should be a tight clearance in the range of 0.03-0.04 mm. Variation in tensile strength of the joint according to the clearance kept between the metallic surfaces to be brazed is shown in Fig. 1 [10, 11].

Due to the manufacturing inaccuracies like ovality in the bore of lugs and outer diameters of tubes, larger clearances become essential to ensure a push-fit assembly. Due to larger clearance in mating parts, capillary action gets affected drastically, thereby reducing the tensile strength of the joint as well as increasing the consumption of brass being the filler metal in the joint.

To improve the tensile strength of the brazed joint, the clearance between the mating surfaces is mechanically reduced by cold compaction of the joint as explained in Section 4. Before the brazing operation, the joint is compacted by a press-tool over a mechanical power press.

This applied research paper is focussed on optimizing the brass consumption during dip brazing of the roadster bicycle frame head joints. Capillary action in the joint had been improved by reducing the joint clearance by mechanical compaction. If the capillary action can be achieved effectively, there is no need to fully submerge the joint in the molten pool of brass. And little dipping of the joint in the molten brass can ensure flow of brass in the entire joint due to the capillary action.

2. Tolerance analysis of the frame head parts

Roadster bicycle frames of lugged type are built with many ERW type cylindrical steel tubes. Two or more tubes are connected to each other through intermediate socket type part called lug. Lug is a component formed from cold drawn steel sheet, which fits over the ends of the steel tubing. Various parts of a typical roadster bicycle frame for men are as shown in Fig. 2 [12].

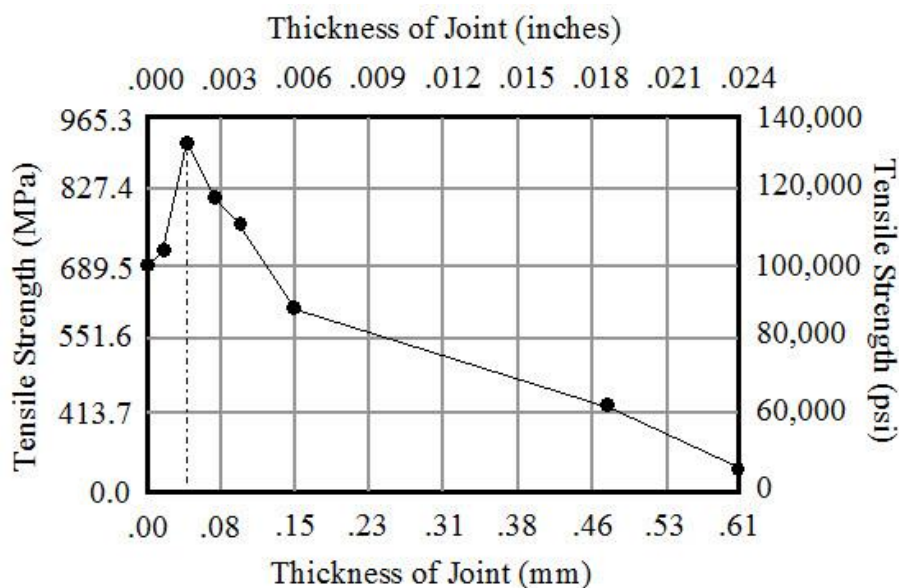


Fig. 1. Effect of joint clearance on tensile strength.

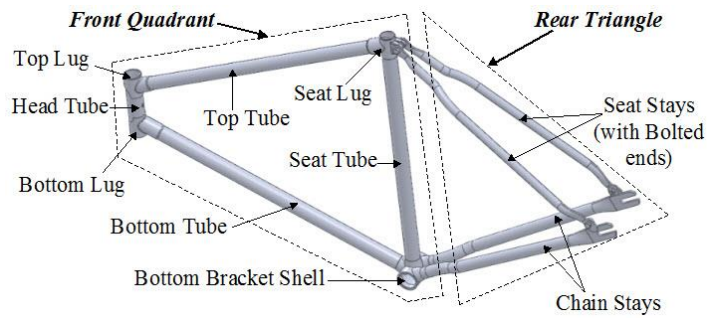
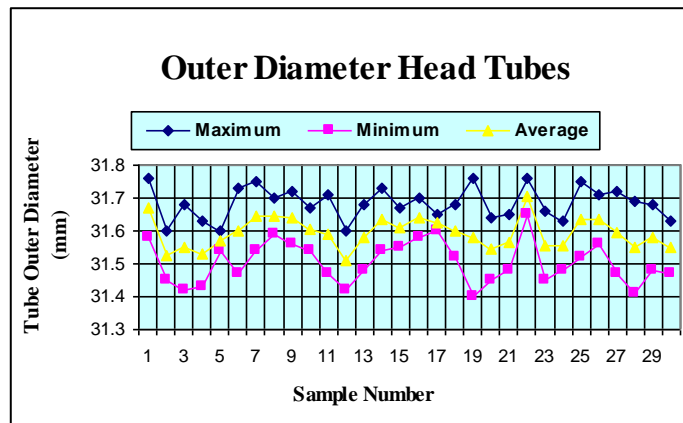
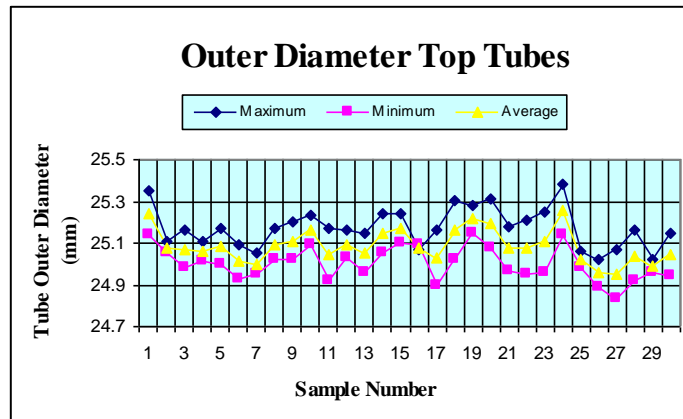


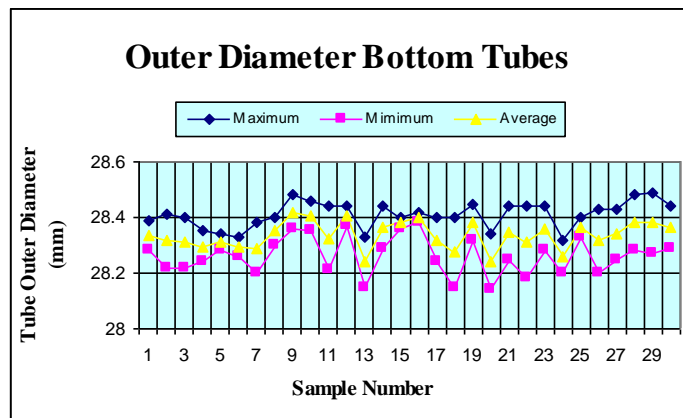
Fig.2 Roadster frame components.
(full colour version available online)



a) Max. of Avg. – 31.71mm ; Min. of Avg. – 31.51mm



b) Max. of Avg. – 25.26mm ; Min. of Avg. – 24.95mm



c) Max. of Avg. – 28.42mm ; Min. of Avg. – 28.24mm

Fig. 3. Measured values of head tubes, top tubes and bottom tubes outer diameters.
(full colour version available online)

Table 2

Tolerance analysis - tube outer diameter in mm.

Tube and Nominal Outer Diameter	Specified limits		Average of Measured Values		Variance	Samples having Variance (%)	Reference Fig. No.
	Max.	Min.	Max.	Min.			
Head Tube ϕ 31.75	31.80	31.62	31.71	31.51	0.11	66.70	3a
Top Tube ϕ 25.40	25.40	25.27	25.26	24.95	0.32	96.70	3b
Bottom Tube ϕ 28.57	28.60	28.44	28.42	28.24	0.20	100.00	3c

Bold face "Average Measured Values" are beyond the specified limits; OD Means - Outer Diameter

Before making assembly of the joint, the samples of top tube and bottom tubes are cut to the required length within the specified tolerance. Then each end of the tube is cut to the shape by "Mitering" [13], so that it can rest closely against the side of the adjoining head tube, at an angle prescribed in the frame assembly. There are many methods of mitering the ends of the tubes, for instance milling, laser cutting, and coping or profile shearing using press tools. Coping is a much faster method to shape the ends of the tubes with fair degree of accuracy and is used in roadster bicycle frame tubes. The tubes with mitered ends are then push fitted into the respective lugs using pneumatically operated assembly fixture. For ease of assembly, using mass production assembly fixtures, and at the same time ensuring a reasonably tight fit assembly of tubes in the lugs, it is essential to keep an effective clearance 0.3-0.4 mm in the joint.

In order to confirm the development of sufficient capillary force during brazing, it is essential to know the true value of clearances in the joints formed when tubes are assembled in the respective lugs. This was done through a detailed tolerance analysis exercise as explained in Section 2.1, 2.2 and 2.3.

2.1 Tolerance analysis of tubes

Circularity of external diameters of head tube, top tube and bottom tube was practically measured on thirty samples of each type of tubes, randomly drawn from the mass production line. Average of maximum and

minimum measured value of tube external sizes were calculated for every sample and the results are plotted in the graph shown in Fig. 3.

20 out of 30 samples (66.7 %) of head tube outer diameters were observed to be beyond the specified limits of 31.62 - 31.78 mm as shown in Fig. 3a.

29 out of 30 samples (96.7%) of top tube outer diameters were observed to be beyond the specified limits of 25.27 – 25.43 mm as shown in Fig. 3b.

30 out of 30 samples (100%) of bottom tube outer diameters were observed to be beyond the specified limits of 28.44 – 28.70 mm as shown in Fig. 3c. Results of Tolerance analysis showing the variations in the calculated average sizes as against the specified limits are shown in Table 2.

2.2 Tolerance analysis of frame head lugs

Similarly, circularity in socket bores of top lug and bottom lug was practically measured on thirty samples of each type of lugs, randomly drawn from the mass production line. Averages of maximum and minimum measured values of lug bore were calculated for every sample and the results are plotted in the graph shown in Fig. 4.

18 out of 30 samples (60 %) of bores in Top Lug for Head Tube were observed to be beyond the specified limits of 31.70 – 31.78 mm as shown in Fig. 4a.

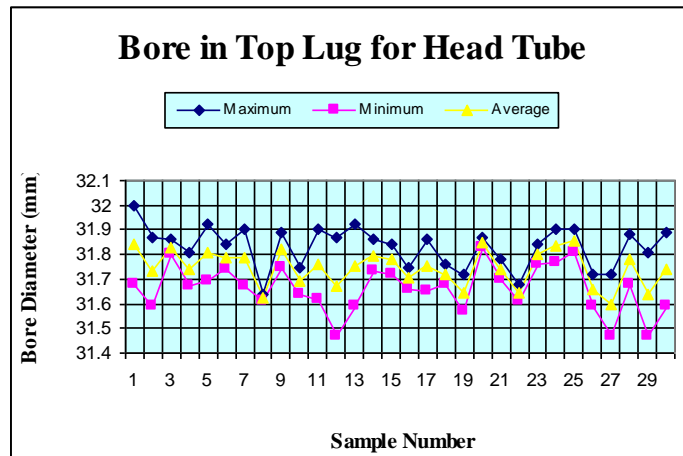
7 out of 30 samples (23.3 %) of bores in Top Lug for Top Tube were observed to be beyond the specified limits of 25.42 – 25.80 mm as shown in Fig. 4b.

11 out of 30 samples (36.7 %) of bores in Bottom Lug for Head Tube were observed to be beyond the specified limits of 31.70 – 31.78 mm as shown in Fig. 4c.

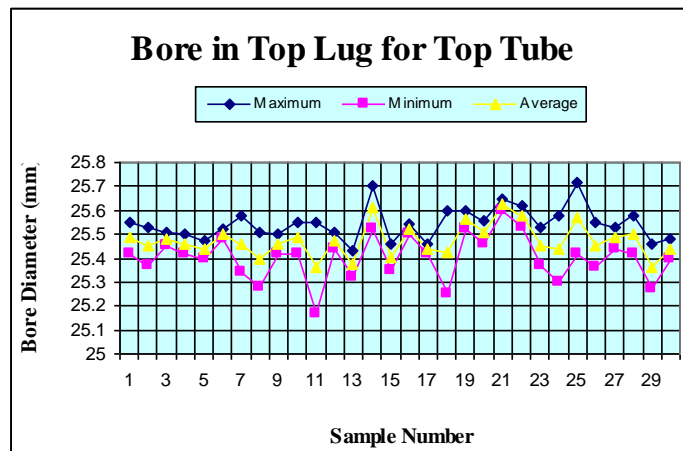
24 out of 30 samples (80 %) of bores in Bottom Lug for Bottom Tube were observed

to be beyond the specified limits of 28.60 – 28.68 mm as shown in Fig. 4d.

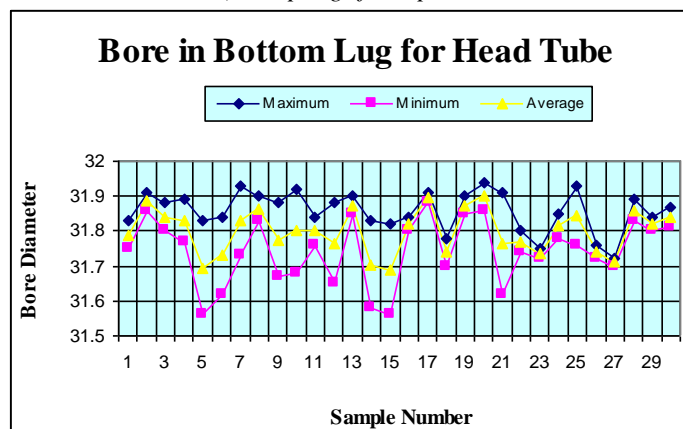
Results of Tolerance analysis showing the variations in the calculated average sizes as against the specified limits are shown in Table 3.



a) in top lugs for head tube

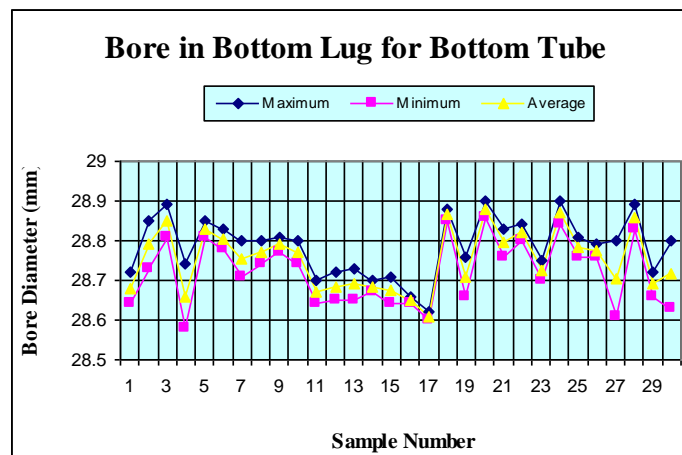


b) in top lugs for top tubes



c) in bottom lugs for head tubes

Fig. 4. Measured values of bore.
(full colour version available online)



d) in bottom lugs for bottom tubes
 Fig. 4. Measured values of tube bore.
 (full colour version available online)

Table 3

Tolerance analysis – lug bore diameter in mm.

Frame Lug and Specified Bore Diameter	Specified limits		Average of Measured Values		Variance	Samples having Variance (%)	Reference Fig. No.
	Max.	Min.	Max.	Min.			
Bore in Top Lugs for Head Tube	31.78	31.7	31.86	31.60	0.08	60	4a
Bore in Top Lugs for Top Tube	25.5	25.42	25.63	25.36	0.13	33.3	4b
Bore in Bottom Lugs for Head Tube	31.78	31.7	31.90	31.69	0.12	36.7	4c
Bore in Bottom Lugs for Bottom Tube	28.68	28.6	28.88	28.61	0.2	80	4d

Bold face “Average Measured Values” are beyond the specified limits; Bore Means – Inner Diameter

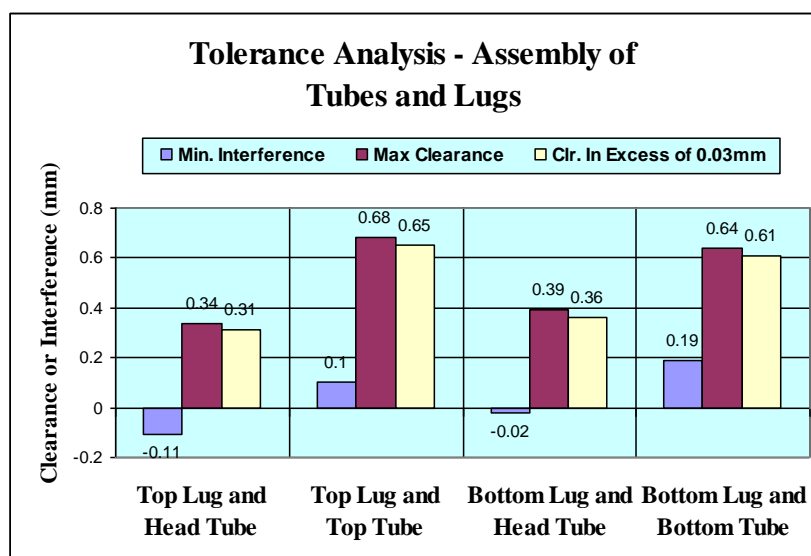


Fig. 5. Tolerance analysis - assembly of tubes and lugs.
 (full colour version available online)

2.3 Tolerance analysis of tubes assembled in frame head lugs

Value of minimum interference, and maximum clearance was computed for the assembly of tubes with respective lugs. Minimum value of interference in the assembly was computed against minimum bore in the lug and the maximum outer diameter of the respective tube, based upon maximum material condition. And maximum clearance in the assembly was computed against maximum bore in the lug and the minimum outer diameter of the respective tube, based upon minimum material condition. Based upon the maximum clearance in the assembly of tubes and respective lugs, clearance in excess of 0.03 mm (being the best design clearance for dip brazing) was computed. Result of the final tolerance analysis of the assembly of tubes with respective lugs is shown in Fig. 5.

Due to large values of clearance in excess of the design clearance of 0.03 mm, between the lugged joints, the desired capillary action during the brazing remains virtually absent. Due to this it is necessary to fully submerge the joint in the molten brass, causing excessive consumption of brass.

2.4 Improvement of capillary action

In order to improve the capillary action during dip brazing, the initial clearance between the lugged joints can be reduced by the following actions.

2.4.1 At the tube design and procurement level

Clearance between the tubes and lugs can be brought down to some extent, by various dimensional control measures. Recommendations were made to narrow down the limits of design tolerance on the outer diameter of ERW tubes to 80 % of the specified tolerances, (within the comfortable limits of customized tube manufacturing) as shown in Table 4.

Table 4

Tube and Nominal Outer Diameter	Proposed tolerances on tube outer diameter. Tolerance on Outer Diameter	
	Existing	Proposed
Head Tube $\phi 31.75$		
Top Tube $\phi 25.40$	(+0.03, -0.13)	(+0.03, -0.1) A bit tighter
Bottom Tube $\phi 28.57$		

2.4.2 At the frame manufacturing process level

Further reduction in clearances between the tubes and lugs is achieved by radial inward compaction of the pre brazed joints of the frame head by a press tool operation.

3. Computation of brass consumption in brazing

Joints namely 1) Head Joint, 2) Seat Lug Joint and 3) Bottom Bracket Shell joint are sequentially dip brazed in roadster bicycle frames [14]. Focus of this paper is on the improvement in dip brazing of the Head Joint as shown in the Fig. 6, being the area of largest consumption of brass among all the three joints.

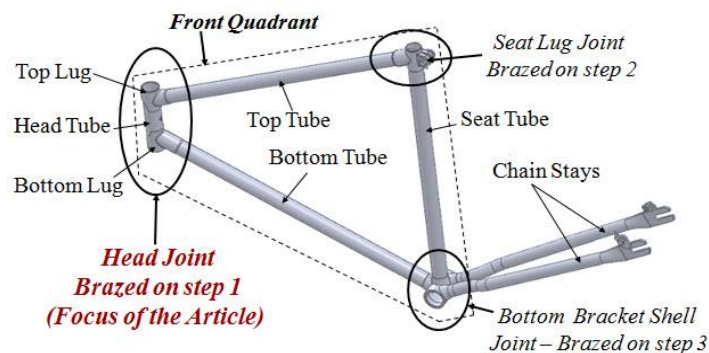
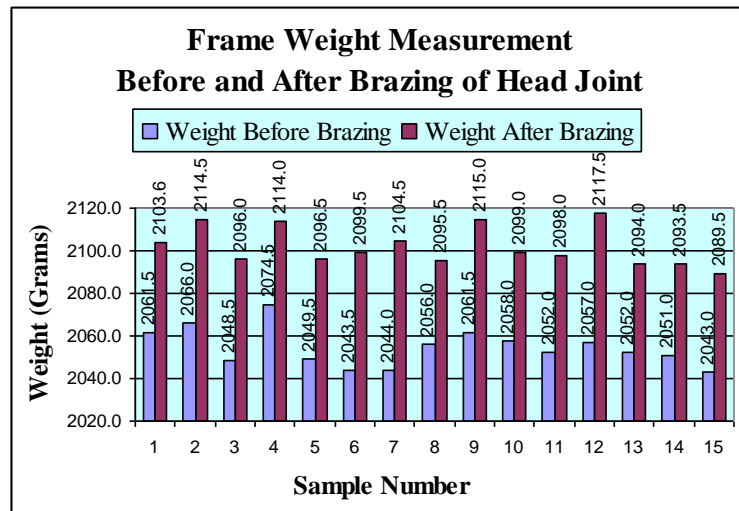


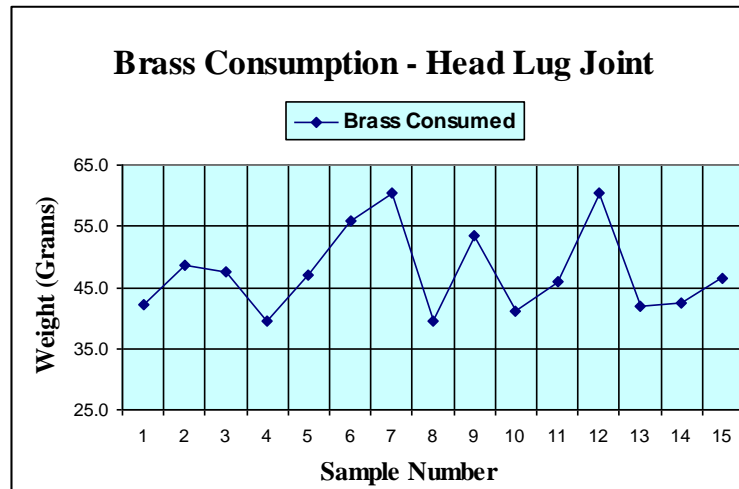
Fig. 6. Roadster frame components. (full colour version available online)



Fig. 7 Dip brazing of head joint. (full colour version available online)



a) frame weight measurement - before and after brazing of head joint



b) brass consumption during brazing of head lug joint

Fig. 8 Computation of brass consumed by weight measurement (full colour version available online)

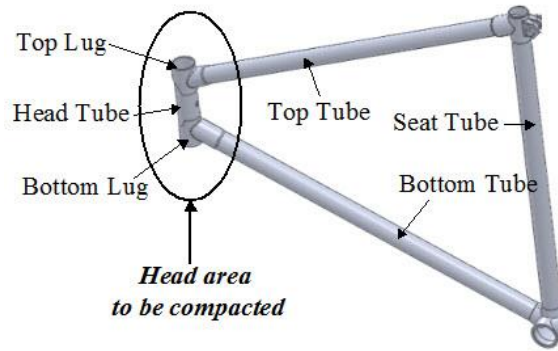
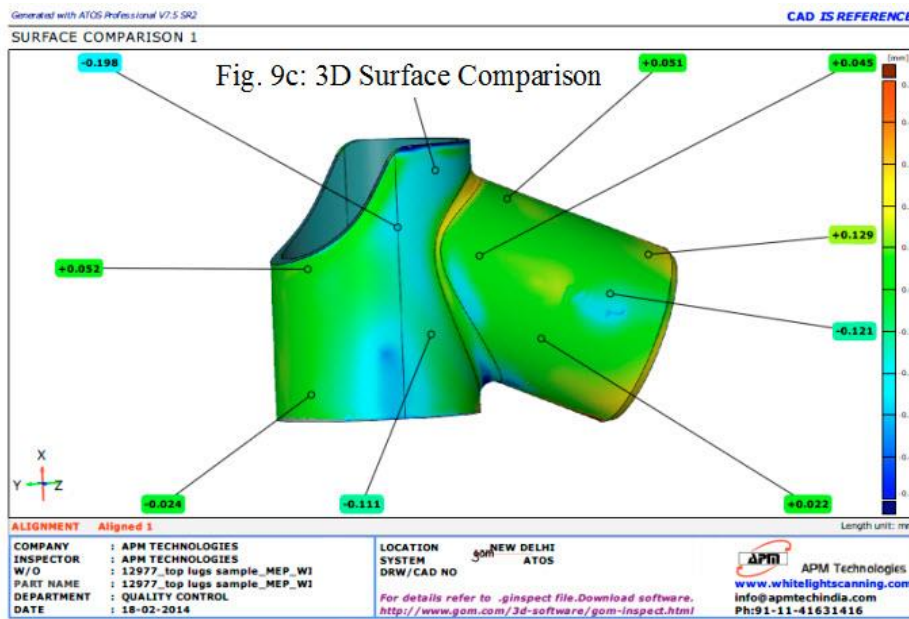
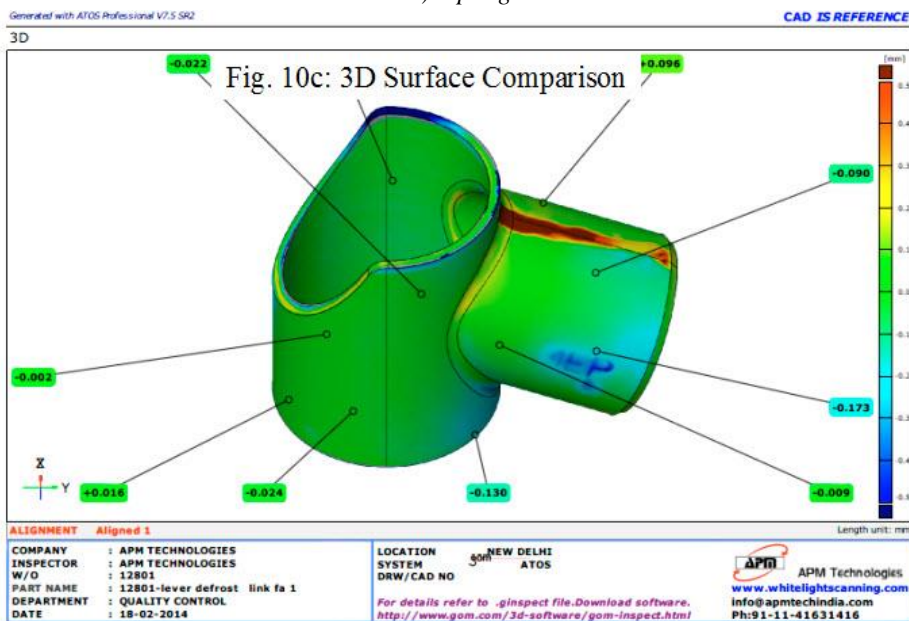


Fig. 9. Head joint area to be compacted. (full colour version available online)



a) top lug



b) bottom lug

Fig. 10. Surface comparison after 3D white light scan. (full colour version available online)

For estimating the brass consumption in brazing, fifteen samples of un-brazed front quadrants, were randomly drawn from the mass production line. Dip brazing was carried out for head joints consisting of “Top-lug joint” (joint of “Head Tube” and the “Top Tube”) and “Bottom lug joint” (joint of “Head Tube” and the “Bottom Tube”) as shown in Fig. 7.

Amount of brass consumed in brazing was computed from the difference in weights of frame before and after the brazing as shown in Fig. 8a.

The results of brass consumption in brazing of head lug joint are shown in Fig. 8b.

4. Compaction of the joints before brazing

Excessive joint clearance between the tubes and the lugs can be most effectively reduced by squeezing the joint dynamically on mechanical power press using a pair of compacting dies. According to the focus of this research paper, the compaction process was demonstrated on head joints as shown in Fig. 9

4.1 Designing of the joint Compaction Dies

The joint can be uniformly squeezed all around, only when a pair of upper and lower dies is produced with their contour of internal surfaces exactly matching with the contour of outside surfaces of the lugs. To transfer

the surface profile of the frame lugs on to the press dies, it is essential to firstly create a 3D profile of outside surfaces of the frame lugs through 3D scanning using white light scanner. Five samples each of “Top Lug” and “Bottom Lug” were randomly drawn from the mass production line. External surfaces of lugs were scanned on White-light 3D scanner at APM Technologies, New Delhi (India). Accuracy of 3D scanning was confirmed through comparison drawn between the actual surfaces of the lugs and the 3D surfaces generated during the white-light scanning as shown in Fig. 10.

Using the external surfaces of 3D solid model of the lugs generated from 3D white-light scan, cavities were produced in the 3D model of the upper and lower die blocks of the compaction die. To avoid stressing of the fillet portions, during the compaction process, fillet radii were increased by 1-2 mm and parting line chamfers were provided on the dies.

Internal surfaces of the compaction die cavities (upper and lower), were selectively offset outwardly in the material addition direction as shown in Table 5, so as to reduce the cavity volume of the die when fully closed. This reduction in the cavity volume, according to the initial clearance of the compaction die, is responsible to squeeze the assembled joint, when the die is fully closed under the mechanical pressure.

Table 5

Initial joint clearance and surface offset in compaction die.

Maximum design joint clearance for capillary action in brazing – 0.0 3mm

Assembly	Max. diametric clearance (mm) (From Fig. 5)	Max. radial clearance (mm)	Surface offset causing material addition in the compaction die (mm)
Top Lug and Head Tube	0.34	0.17	0.14
Top Lug and Top Tube	0.68	0.34	0.31
Bottom Lug and Head Tube	0.39	0.20	0.17
Bottom Lug and Bottom Tube	0.64	0.32	0.29

4.2 Manufacturing of compaction dies and press tool

Upper and lower half of the die blocks were manufactured on CNC vertical machining centre. The die blocks were assembled in a press tool that can be mounted on the power press as shown in Fig. 11. Compaction was done on a hydraulic press (Capacity 60 Tonnes \times stroke 100 mm). For better productivity, compaction can be done on mechanical power press as well.

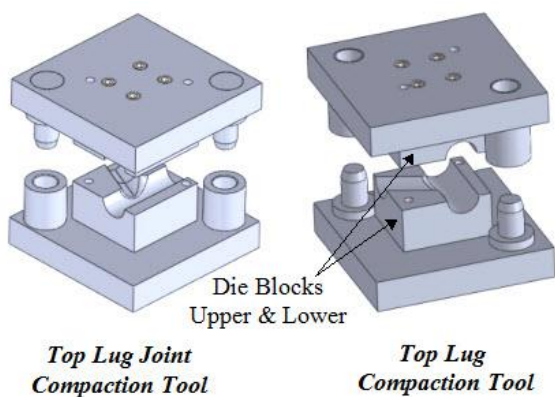


Fig. 11. Compaction press tools for head parts.
(full colour version available online)

4.3 Compaction process

Five sets of L-shaped samples, as shown in Fig. 12, were prepared for compaction trials before the brazing operation. Samples for compaction trials were cut from front quadrants randomly drawn from the production line.

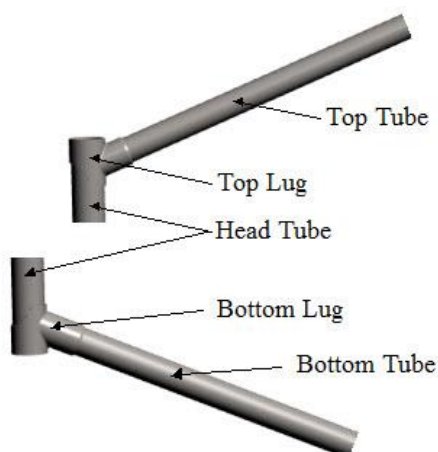


Fig. 12. Samples for joint compaction.
(full colour version available online)

4.4 Flow of material of lug during compaction

Once the assembled joint is radially squeezed from all sides by the mechanical pressure in the press tool, the material of the lug flows plastically in radial and axial directions. The radial flow takes place in inward direction and narrows down the clearance between the lug inner surface and the tube. The radial compaction is compensated by an axial outward flow of the lug material in the free direction. The amount of axial flow of material is quite negligible as compared to the highly significant radial inward flow under the mechanical restraint from the die.

The direction of flow of the “Top Lug” material during compaction process is shown in Fig. 13. Flow of material in the “Bottom Lug” is also on the similar lines.

5. Brazing and testing of compacted joints

5.1 Brazing of samples

Head lug joints were manually dipped in the molten brass in a crucible maintained at a temperature 905-910 °C. The compacted L-shaped samples of the “Top Lug” joint and “Bottom Lug” joint were dipped in the molten bath for a time period of 35-40 seconds. The metallic surfaces of connecting tubes and lugs get brazed together due to the flow of molten filler metal (brass) between them, by the development of capillary force. After this the joint is taken out of the molten bath and is allowed to cool down naturally in air. As the joint cools down, the filler metal (brass) gets hardened and forms a rigid joint between the tubes and the lugs. The head tube was cut from the middle and brazed samples of “Top Lug” joint and “Bottom Lug” joint were separated out. Samples of brazed joints are shown in Fig. 14.

5.2 Tensile strength testing

Tensile strength of each brazed joint between and the respective lug was done. Five sets each of L-shaped test samples

of the “Top Lug” joint and “Bottom Lug” joint were prepared. The tensile tests were carried out on 40Tonnes capacity universal testing machine. The fixture used for tensile testing the samples is shown in Fig. 15.

During the tensile test, all the samples displayed a ductile fracture with neck formation from the middle of the longer tube (Top tube or Bottom tube) as shown in Fig. 16. The brazed joint did not display any type of fracture. Thus it was concluded that the brazed joints were stronger in tension than the parent tubes.

Breaking loads for the samples of head lug joints is shown in Table 6.

Table 6

Breaking loads in tension – head lug Joints.

Top Lug Joints		Bottom Lug Joints	
Sample No.	Breaking Load (N)	Sample No.	Breaking Load (N)
1	47880	1	36960
2	47760	2	36940
3	50260	3	36820
4	47640	4	36120
5	47560	5	36320
Max.	50260	Max.	36960
Min.	47560	Min.	36120
Average	48656	Average	36468

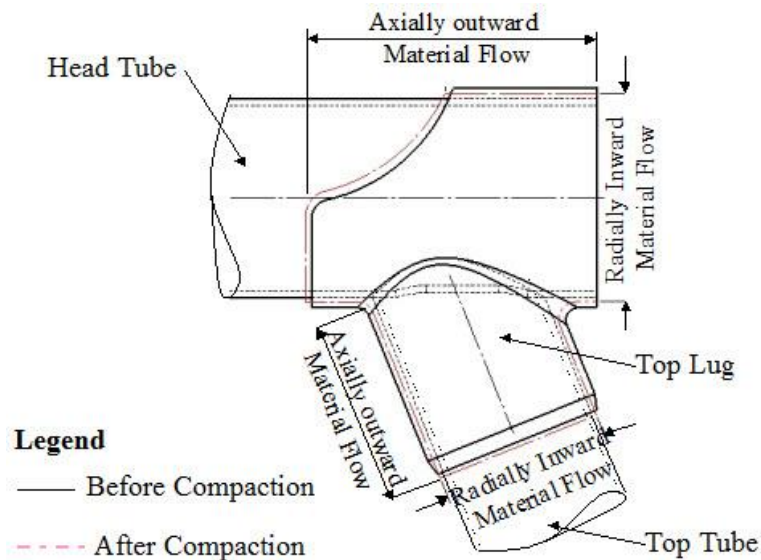


Fig. 13. Flow of materials during compaction.
(full colour version available online)

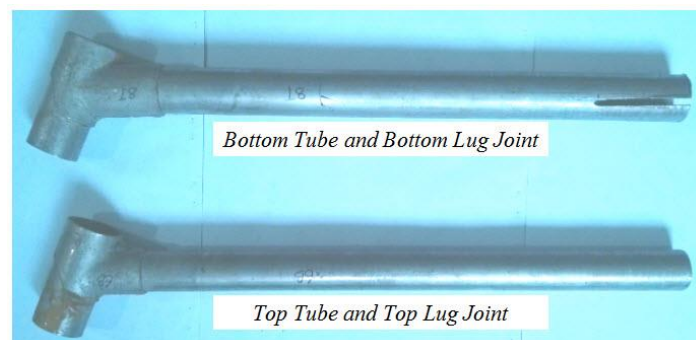


Fig. 14. Samples of joints for testing of tensile strength on universal testing machine.
(full colour version available online)

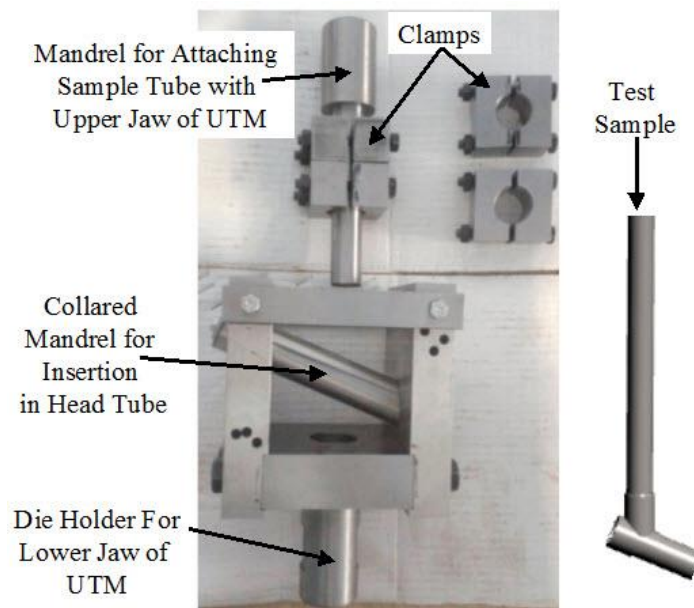


Fig. 15. Testing fixture and test sample for use on universal testing machine.
(full colour version available online)

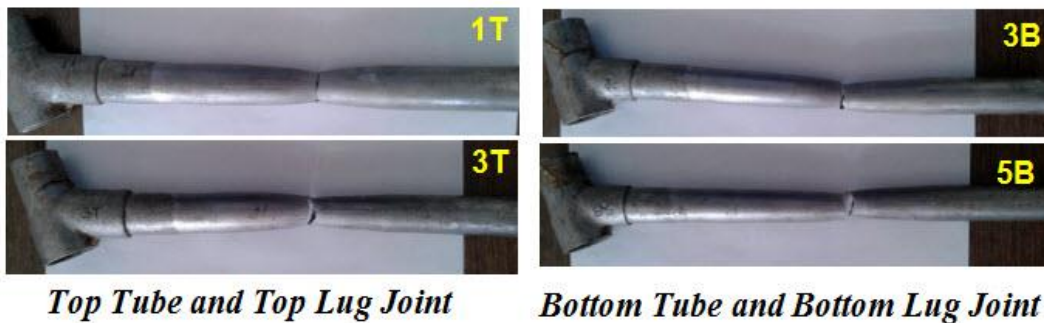


Fig. 16. Brazed joint samples tested on universal testing machine.
(full colour version available online)

5.3 Measurement of brazing layer thickness

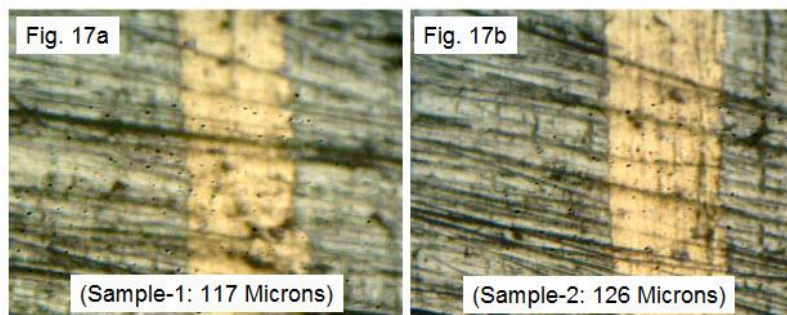
The “Top Lug” joint and “Bottom Lug” joint samples used in the tensile strength testing were sectioned across the central plane. The sectioned samples were ground flat, polished and etched to enable microscopic measurement of brazing layer thickness on an inverted microscope. Results of microscopic measurement of thickness of brass layer, under a magnification of 100× for “Top Lug Joint” is shown in Fig. 17.

Results of microscopic measurement of thickness of brass layer, under a magnification of 100× for “Bottom Lug Joint” is shown

in Fig. 18.

Comparison was drawn among joint clearance before compaction and after the brazing followed by compaction. The results of reduction in joint clearance due to compaction are shown in Table 7.

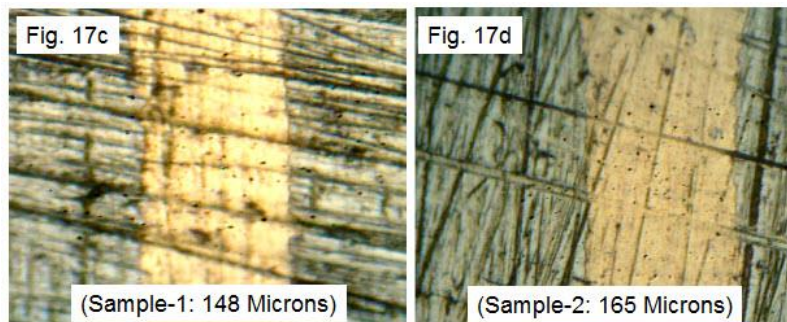
We can find some variance in measured thickness of brazing and the amount of radial compaction actually introduced in the compaction die. The variation in clearance is primarily due to 1) spring-back of the sheet formed lugs during press operation 2) inaccuracies during manufacturing of the compaction die.



Top Lug and Head Tube

a) sample 1 top lug and head tube

b) sample 2 top lug and head tube

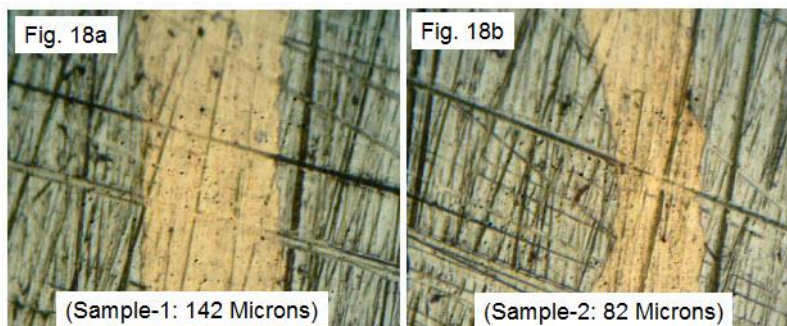


Top Lug and Top Tube

c) sample 1 top lug and top tube

d) sample 2 top lug and top tube

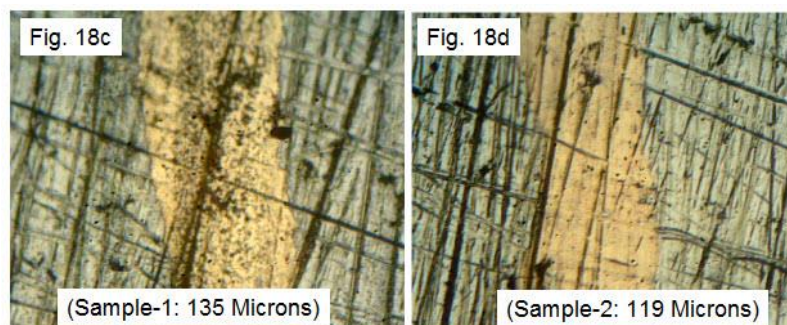
Fig. 17. Brazing layer thickness in top lug joint.
(full colour version available online)



Bottom Lug and Head Tube

a) sample 1 bottom lug and head tube

b) sample 2 bottom lug and head tube



Bottom Lug and Bottom Tube

c) sample 1 bottom lug and top tube

d) sample 2 bottom lug and top tube

Fig. 18. Brazing layer thickness in bottom lug joint.
(full colour version available online)

Table 7

<i>Joint clearance reduction after compaction (mm).</i>						
Sr.	Assembly	<i>Joint Clearance before compaction</i>	<i>Minimum brazing thickness after compaction</i>		<i>Reduction in joint clearance after compaction</i>	
		<i>(As in Table 5)</i>	<i>Values in 2 samples</i>	<i>Average</i>	<i>Values in 2 samples</i>	<i>Average</i>
A	B	C	D	E	F	G
1	Top Lug and Head Tube	0.34	0.117 0.126	0.122	0.223 0.214	0.218
2	Top Lug and Top Tube	0.68	0.148 0.165	0.157	0.532 0.515	0.524
3	Bottom Lug and Head Tube	0.39	0.142 0.082	0.112	0.248 0.308	0.278
4	Bottom Lug and Bottom Tube	0.64	0.135 0.119	0.127	0.505 0.521	0.513

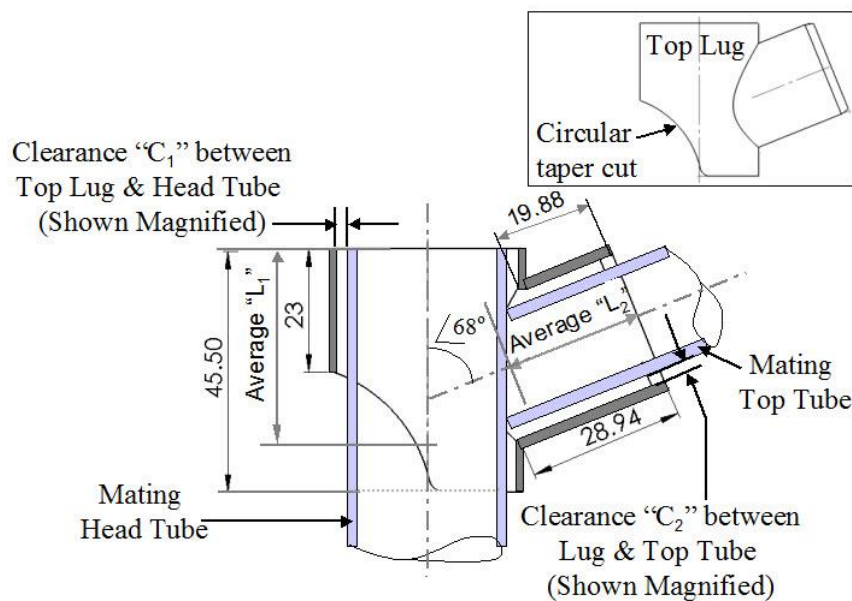


Fig.19. Volume of brass layer in top lug joint.
(full colour version available online)

6. Optimization of the brass consumption

Consumption of brass in brazing is directly proportional to the clearance between the joint. Hence to reduce the brass consumption it is necessary to reduce the joint clearance by squeezing the joint mechanically from all sides.

Quantity of brass – filler material trapped between the mating surfaces of the joint

is estimated. Volumetric calculations of brass based upon the contact area between the lugs and the tubes are as under.

6.1 Volumetric calculations for Top Lug Joint

Various dimensions of “Top Lug” which are having relationship with contact area between the mating tubes are shown in Fig. 19. The clearances “C₁” – between

the lug and the “Head Tube” and “C₂” – between the lug and the “Top Tube” have been shown magnified for clarity. First of all average lengths of engagement “L₁” and “L₂” of socket of the lug covering each tube is calculated from the maximum and minimum lengths of the trapezoidal-cut lugs.

Nominal outside diameter of the “Head Tube” (DH) = 31.75 mm.

Nominal outer diameter of the “Top Tube” (DT) = 25.4 mm.

Average length of cylindrical socket covering “Head Tube” {Term “L₁” as shown in Fig. 19} = (45.5 + 23) / 2 = 34.25 mm.

Average length of cylindrical socket covering “Top Tube” {Term “L₂” as shown in Fig. 19} = (28.94 + 19.88) / 2 = 24.41 mm.

6.1.1 Computation of joint clearance volume before compaction

Maximum clearance between “Top Lug” bore and “Head Tube” outside diameter {(Term “C₁” as shown in Fig. 19) and value as per Fig. 5} = 0.34 mm.

Clearance volume of cylindrical socket covering “Head Tube” (V₁) = π×DH×L₁×C₁ = π×31.75×34.25×0.34 = 1161.5 mm³.

Maximum clearance between “Top Lug” bore and “Top Tube” outside diameter {(Term “C₂” as shown in Fig. 19) and value as per Fig. 5} = 0.68 mm.

Clearance volume of cylindrical socket covering “Top Tube” (V₂) = π×DT×L₂×C₂ = π×25.4×24.41×0.68 = 1324.5 mm³.

Total Clearance volume for both the sockets of the “Top Lug” joint = (V₁) + (V₂) = 1161.5 + 1324.5 = 2486 mm³. (A)

6.1.2 Computation of joint clearance volume after compaction and Brazing

Joint brazing thickness between “Top Lug” and “Head Tube” {Cell value (E₁) - as per Table 7} = 0.122 mm.

Brazing volume of “Top Lug” socket covering “Head Tube” (V₃) = π×DH×L₁×E₁ = π×31.75×34.25×0.122 = 416.78 mm³.

Joint brazing thickness between “Top Lug” and “Top Tube” {Cell value (E₂) - as per Table 7} = 0.157 mm.

Brazing volume of “Top Lug” socket covering “Top Tube” (V₄) = π×DT×L₂×E₂ = π×25.4×24.41×0.157 = 305.8 mm³.

Total brazing volume for both the sockets of the “Top Lug” joint = (V₃) + (V₄) = 416.78 + 305.8 = 722.6 mm³. (B)

Volume of brass saved in brazing due to compaction of “Top Lug” joint = (A) - (B) = 2486 – 722.6 = 1763.4 mm³.

Density of 60:40 Brass = 8.525 g·cm⁻³.

Reduction in consumption of brass in brazing after compaction of “Top Lug” joint = (1763.4×8.525) / 1000 = 15.1 g. (C)

6.2 Volumetric calculations for Bottom Lug Joint

Various dimensions of “Bottom Lug” which are having relationship with contact area between the mating tubes are shown in Fig. 20. The clearances “C₃” – between the lug and the “Head Tube” and “C₄” – between the lug and the “Bottom Tube” have been shown magnified for clarity. First of all average lengths of engagement “L₃” and “L₄” of socket of the lug covering each tube is calculated from the maximum and minimum lengths of the trapezoidal-cut lugs.

Nominal outside diameter of the “Head Tube” (DH) = 31.75 mm.

Nominal outer diameter of the “Bottom Tube” (DB) = 28.57 mm.

Average length of cylindrical socket covering “Head Tube” {Term “L₃” as shown in Fig. 20} = (47 + 27.39) / 2 = 37.2 mm.

Average length of cylindrical socket covering “Bottom Tube” {Term “L₄” as shown in Fig. 20} = (39.78 + 26.26) / 2 = 33.02 mm.

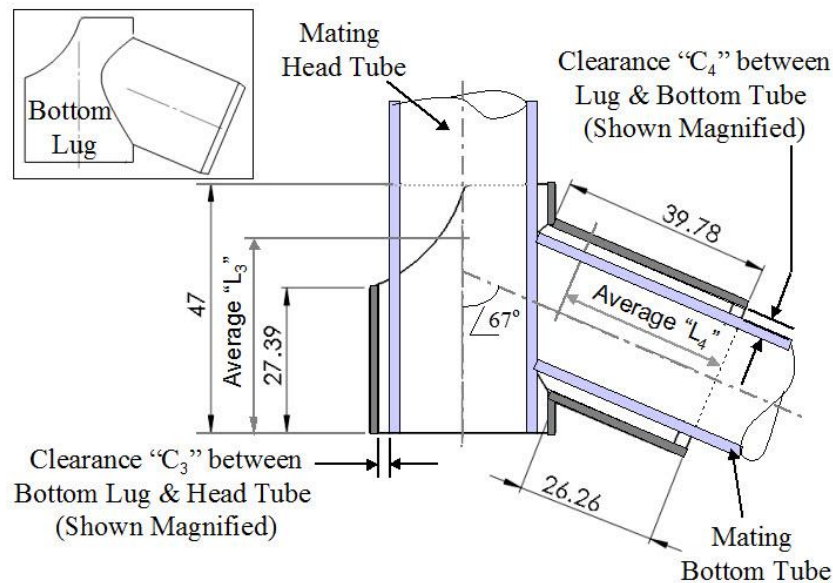


Fig. 20. Volume of brass layer in bottom lug joint.
(full colour version available online)

6.2.1 Computation of joint clearance volume before compaction

Maximum clearance between “Bottom Lug” bore and “Head Tube” outside diameter {(Term “C₃” as shown in Fig. 20) and value as per Fig. 5} = 0.39 mm.

Clearance volume of cylindrical socket covering “Head Tube” (V_5) = $\pi \times DH \times L_3 \times C_3$ = $\pi \times 31.75 \times 37.2 \times 0.39$ = 1447.1 mm³.

Maximum clearance between “Bottom Lug” bore and “Bottom Tube” outside diameter {(Term “C₄” as shown in Fig. 20) and value as per Fig. 5} = 0.64 mm.

Clearance volume of cylindrical socket covering “Bottom Tube” (V_6) = $\pi \times DB \times L_4 \times C_4$ = $\pi \times 28.57 \times 33.02 \times 0.64$ = 1896.8 mm³.

Total Clearance volume for both the sockets of the “Bottom Lug” joint = (V_5) + (V_6) = 1447.1 + 1896.8 = 3343.9 mm³. (D)

6.2.2 Computation of joint clearance volume after compaction and brazing

Joint brazing thickness between “Bottom Lug” and “Head Tube” {Cell value (E₃) - as per Table 7} = 0.112 mm.

Brazing volume of “Bottom Lug” socket covering “Head Tube” (V_7) = $\pi \times DH \times L_3 \times E_3$ = $\pi \times 31.75 \times 37.2 \times 0.112$ = 415.6 mm³.

Joint brazing thickness between “Bottom Lug” and “Bottom Tube” {Cell value (E₄) - as per Table 7} = 0.127 mm.

Brazing volume of “Bottom Lug” socket covering “Bottom Tube” (V_8) = $\pi \times DB \times L_4 \times E_4$ = $\pi \times 28.57 \times 33.02 \times 0.127$ = 376.4 mm³.

Total brazing volume for both the sockets of the “Top Lug” joint = (V_7) + (V_8) = 415.6 + 376.4 = 792 mm³. (E)

Volume of brass saved in brazing due to compaction of “Bottom Lug” joint = (D) - (E) = 3343.9 - 792 = 2551.9 mm³.

Density of 60:40 Brass = 8.525 g·cm⁻³.

Reduction in consumption of brass in brazing after compaction of “Bottom Lug” joint (2551.9 x 8.525) / 1000 = 21.8 g (F).

Total reduction in consumption of brass in brazing after compaction of the head part of the frame = (C) + (F) = 15.1 + 21.8 = 37.9 g (G).

The brass consumption as in (G) above can be compared against the existing average

brass consumption of 47.5 grams as shown in Fig. 8b.

7. Conclusion and recommendations

7.1 Conclusion

It can be concluded that by carefully planned mechanical compaction of the tube and socket joint,

- a) the joint clearance can be substantially reduced,
- b) better capillary action can be achieved for an improved flow of brass,
- c) partial dipping of the joint in molten brass is able to cause adequate flow of brass,
- d) consumption of brass can be reduced, without sacrificing the joint strength.

7.2 Recommendations

It is recommended to carry out more research to establish the extra amount of radial compaction in the die to compensate the spring-back action in the material of the sheet formed lugs, after removal of the compacting force by the die. Such an amount of extra compaction needs to be established by more iterative practical trials.

If need be, more number of stages of compaction to be added in the process, if compaction beyond 0.35 mm becomes necessary (to achieve 0.03-0.04 mm clearance ideally suited for an effective capillary action required for dip brazing).

It is recommended to extend the process of joint compaction in “Seat lug” joint and “Bottom Bracket” joint as well.

It is recommended to use the sheet formed lugs that are within the prescribed tolerance limits of +0.08 mm on the bore diameter.

It is further recommended to narrow down the tolerance on the outer diameter of steel tubes to +0.03-0.10 mm as described in Table 4, to optimize the initial clearance in the joints.

Acknowledgements

The authors are highly indebted to;

1) Hero Cycles Limited, Ludhiana (India) - largest manufacturer of bicycles of India, for providing infrastructure support. Engineers namely Mr. Raj Kumar Rattan, Mr. Chaman Singh and Mr. NK Jindal made valuable contribution in carrying out the trials on the shop floor.

2) Members of faculty namely Er. Pushpinderjit Singh, Er. Ravinder Kumar and Mr. Deepak Sharma from the Department of Mechanical Engineering, Ludhiana College of Engineering and Technology, Ludhiana (India) for dedicated support in the research.

3) APM Technologies, New Delhi (India), for White-light 3D scanning of lugs.

References

- [1] Dip brazing, available on: <http://www.dipbraze.com/what-is-dip-brazing>.
- [2] M.M. Schwartz: Brazing, 2nd edition, ASM International, USA, OH 2011.
- [3] Classic roadster bicycles, available on: [https://en.wikipedia.org/wiki/Roadster_\(bicycle\)#Gents.27_roadster](https://en.wikipedia.org/wiki/Roadster_(bicycle)#Gents.27_roadster). 9J.R. Davis: ASM Materials Engineering Dictionary, ASM International Ohio 1992.
- [4] IS 623 (2008): Bicycle – Bicycle frames. Indian standard.
- [5] A. Holden, B. Sammler, B.L Powers, S.A. Schmidt: Structural Design for the Stage, CRC Press 2013.
- [6] Steel Tubes for Bicycles and Cycle Rickshaws – Specifications, Indian Standard, IS-2039 (Part-3), 1993.
- [7] Hot Rolled Carbon Steel Sheet and Strip – Specifications, 6th Edition, Indian Standard, IS-1079, 2009.
- [8] T. Lyman: Metals handbook, American society for metals, Cleveland 1948.
- [9] J.R. Davis: ASM Materials Engineering Dictionary, ASM International Ohio 1992.
- [10] R.H. Leach: Effect of joint clearance on tensile strength, 1939, available on: <https://vacaero.com/information-resources/vacuum-brazing-with-dan-kay/1300-the-famous-joint-strength-vs-joint-clearance-chart.html>.

- [11] A.Kh. Al Taie, A.A. Ateia: JKAU: Eng. Sci.18(1) (2007) 57-72.
- [12] M. A. R. Chimonas: In: Lugged Bicycle Frame Construction, Create Space Independent Publishing Platform 2013, pp. 8-12.
- [13] G. Miller: Tube Forming Processes: A Comprehensive Guide, Society of Manufacturing Engineers 2003.
- [14] H. R. Brooker, E. V. Beatson: Industrial Brazing, Iliffe and Sons Ltd, London 1953.



EVALUATION OF WEAR BEHAVIOR OF Al-Si ALLOY USING SiC AS THE REINFORCEMENT

Amit Handa^{1,*}, Vikas Chawla²

¹ I.K.G. Punjab Technical University Campus, Hoshiarpur, (Punjab) India.

² Ferozpur College of Engineering & Technology, Feroz-shah, (Punjab) India.

*corresponding author: e-mail: handaamit_2002@yahoo.com

Resume

The current study investigates the wear behavior of the SiC particles reinforced Al-Si alloy composites developed using the stir casting process. The results were obtained from the wear tests of the cast Al-Si alloy and prepared SiC reinforcement composites containing 3 % wt and 9 % wt using fine and coarse size SiC particles. The wear test of all the developed composites were done at different testing conditions with varying loads. The analysis of wear traces, as well as the wear debris, was done at every composition but at higher loads. It was observed that the wear resistance was improved with increasing the amount as well as decreasing the size of the SiC particles. However, the wear rate of the composites increases with increasing the applied load. From the microstructural study of specimen after the wear test one can conclude that both adhesive and abrasive wear mechanisms contribute for wear of SiC particle composites.

Article info

Article history:

Received 21 February 2016

Accepted 15 October 2016

Online 04 February 2017

Keywords:

Al-Si alloy;

Stir casting;

Wear track;

Wear debris.

Available online: <http://fstroj.uniza.sk/journal-mi/PDF/2016/18-2016.pdf>

ISSN 1335-0803 (print version)

ISSN 1338-6174 (online version)

1. Introduction

The investigation of friction and wear caught the attention of many scientists during the course of the last few decades, however, consistent and sustained scientific investigation into friction and wear is a relatively recent phenomenon. The concept of developing special materials and coatings to overcome friction and wear problems is becoming a reality. Composites are the class of material that evolved with the existence of nature. Nature inspires the today's composite advancement in the field of aeronautical, aerospace, automotive and structural sector. Composites are engineered materials that have been designed to provide significantly higher specific stiffness and specific strength i.e. higher structural efficiency relative to previously available structural materials. As a common practical definition, composite materials may be restricted to emphasize those materials that contain a continuous matrix constituent that

binds together and provides form to an array of a stronger, stiffer reinforcement constituent. The resulting composite material has a balance of structural properties that is superior to either constituent material alone [1]. Reinforced concrete is an excellent example of a composite structure in which the concrete and steel still retain their identities.

Das et al. [2] proposed that some of the aluminum alloys exhibit wide range of properties but lacks in tribological properties, which limits its use to certain applications. Das et al. [3] have developed an aluminum matrix composite with reinforcement of hard particles that is the widely used option for enhancing tribological properties as compared to other techniques, in terms of ease and economics involved along with the achievement of desired properties.

2. Experimentation

In the present work, aluminum alloy was chosen as the matrix material due to its light

Table 1

Nominal (NCC) and actual (ACC) chemical composition of the aluminum alloy.

Elements	Si	Fe	Cu	Mn	Mg	Zn	Ni	Al
NCC	10-12	1	0.7-1.4	0.5	0.8-1.5	0.2-0.5	1.0-1.5	Bal.
ACC	11.8	0.6	1.1	---	1.3	0.2	1.3	Bal.

weight with good corrosion resistance. SiC has been used as the reinforcement material because of high hardness, high modulus of elasticity with good thermal stability. The chemical composition of the aluminum alloy is presented in Table 1.

Effect of the reinforced SiC particle size on the wear behavior of the composites is monitored in the present work. For this purpose two ranges of sizes were selected for the reinforcement: fine size and coarse size.

In the present investigation, stir casting technique is used for the development of the composite. This process involves the mixing of the particles into aluminum melt with the help of the stirrer and then allows the material to solidify in the mold at the normal environmental conditions [4]. Afterwards, the melt was transferred to the metal mold of cast iron of dimension $0.1 \times 0.1 \times 0.05$ m and then allowed to solidify at room temperature. The samples were prepared by using SiC reinforcement of 3 %, and 9 % (by weight) with fine and coarse particles.

3. Characterization

The dry sliding wear test, using the pin-on-disc method, was done to study the wear behavior of the prepared composite. The samples of the cast composite were machined to 8 mm diameter cylindrical pins and the wear tests were performed on pin on disc under the dry sliding conditions in ambient air at controlled temperature. The wear tests were conducted at different loads (9.8 N, 19.6 N, 29.4 N, 39.2 N and 49 N). All the aluminum composite samples were tested against EN32 steel disc having 65HRC hardness. Average value of the wear rate was calculated bases on three observations by taking run three times.

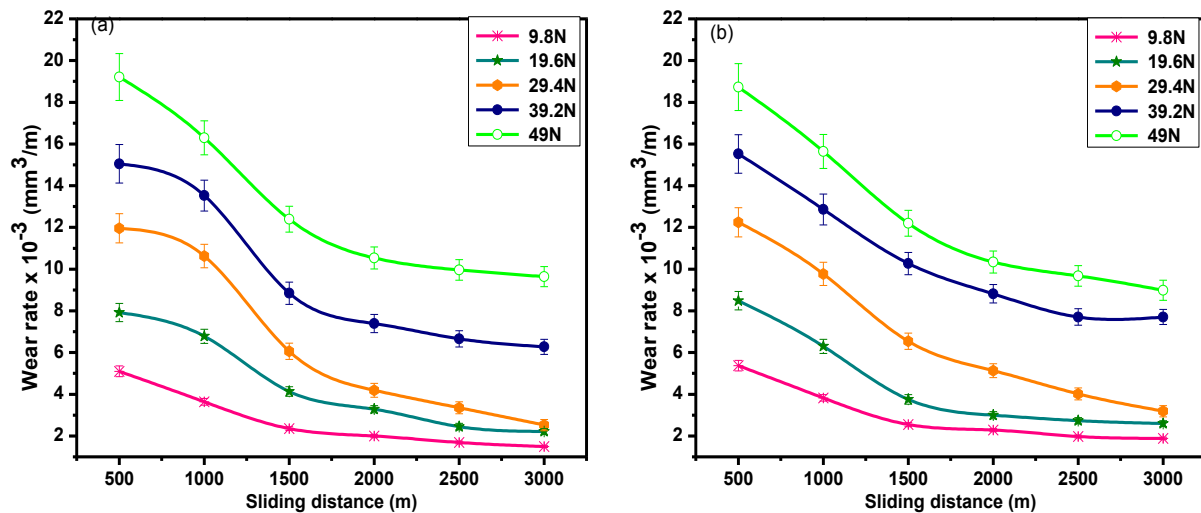
Before each test, the track was properly cleaned with acetone. All the wear tests were conducted on the new wear tracks in order to get similar test conditions. A constant sliding velocity of 1.75 m s^{-1} was maintained throughout the experiment and sliding distance covered during the experiment was about 3000 meters.

4. Results and Discussion

4.1 Effect of load on the wear behavior

Figs. 1 and 2 shows the variation of wear rate with sliding distance at different applied loads for the composites having 3 and 9 wt. % of fine and coarse size SiC particles, respectively. The wear rate of 3 wt. % fine and coarse size reinforced composite, as a function of sliding distance at variable loads from 9.8 N to 49 N is shown in Fig. 1a-b. The wear rate in the composites is observed to increase with increasing load. However, the 3 wt. % fine size reinforced composite (Fig. 1a) shows a minimum wear rate. In the initial stages of run, the abrasive wear between the two surfaces in relative motion is dominant. The abrasive wear is controlled by the asperity to asperity contact of the two surfaces. The pin specimen of the composite and the hard steel counter surface contains large asperities of different height, shape and sharpness [5].

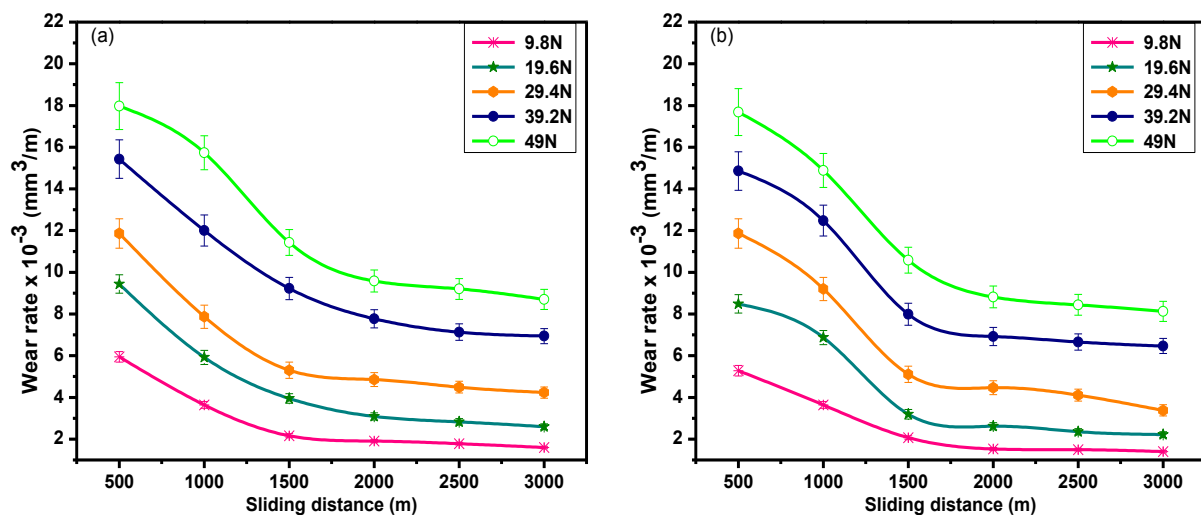
Some of the protruded asperities of the hard surface may penetrate into the softer pin. Subsequent sliding due to the reciprocating motion leads to the removal of material. The abrasive wear is accompanied by the formation of thin and shallow grooves on the specimen. So the initial stages of run have shown very heavy wear loss due to the statistical fluctuations in wear. The continuous grinding of these abrasive particles while sliding reduces the sharpness of the asperities. These blunt



a) fine size reinforced

b) coarse size reinforced

Fig. 1. The wear rate of composites against sliding distance at different loads for 3 wt. %
(full colour version available online)



a) fine size reinforced

b) coarse size reinforced

Fig. 2. The wear rate of composites against sliding distance at different loads for 9 wt. %
(full colour version available online)

shaped smooth abrasives cause fall in the wear loss and the steady state is attained. The similar type of wear behavior is also observed by Chaudhary et al. [6] and Onat [7]. The continuous increase in the wear rate is observed in all the composites with the increase in load from 9.8 N to 49 N. Application of the high load causes huge removal of material, which may be explained based on plastic deformation. The oxide film,

which acts as a cover envelope to the metal surface, breaks during the dry sliding, thus bringing the surfaces in contact.

On increasing the amount of SiC particles in the composite from 3 to 9 wt. % further reduction in wear rate is observed as shown in Fig. 2a-b. Improvement of the wear resistance with increasing the amount of SiC particles from 3 wt. % to 9 wt. % was observed at all applied loads.

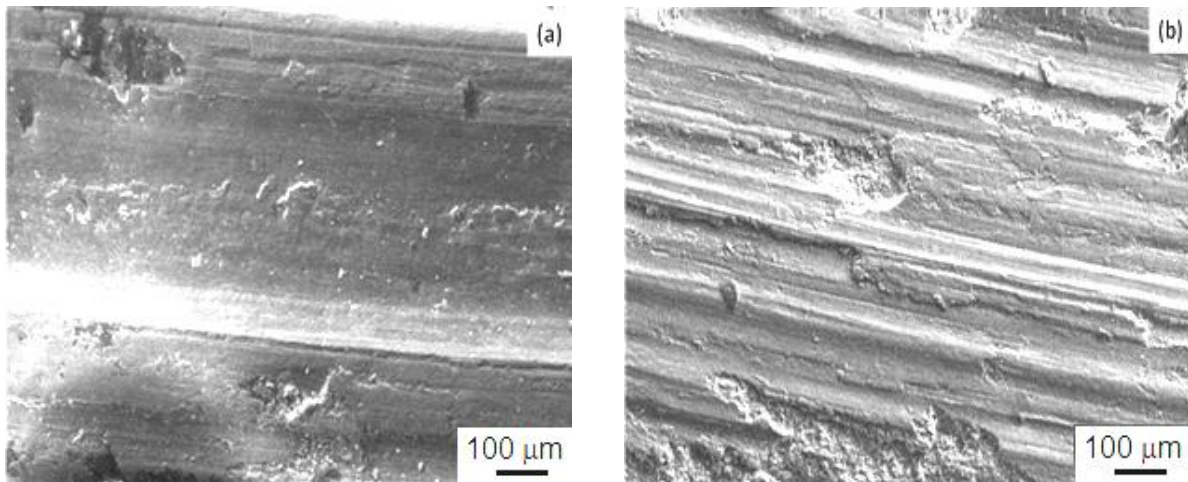
The high wear rate of the material during the run in wear stage was observed for the 9 wt. % coarse size SiC particles composite because the coarse size SiC particles have smaller surface area as compared to the fine size SiC particle inside the composites. The large surface area of fine size SiC particles increases the interfacial area [5]. This, in turn, increases the brittleness and enhances the hardness of the 9 wt. % SiC particles composite. The improvement in wear resistance can be attributed to the increased hard SiC particle addition, which restricts the damage from the abrasives of the counter surface, which is evident from the graph even at higher applied loads of 49 N.

4.2 Analysis of wear traces at applied peak loads

The removal of the material from the contacting surface during the dry sliding conditions leaves numerous permanent impressions on the surface of the composites. A careful investigation of the wear traces and the wear debris help to understand the wear mechanism. The particular type of wear which is responsible for the wear loss depends upon the various factors like the sliding speed, sliding distance, applied load and frictional temperature at which wear tests are performed, [8]. The SEM micrographs of the wear traces of composites, containing different size and amount of the SiC particles, tested at 49 N loads, are presented in the Figs. 3 and 4. The scar on the sliding surfaces suggests that the abrasive wear is the dominating mechanism under these conditions. The asperities of the contacting surfaces undergo plastic deformation during sliding due to the normal stress, [9]. The high local pressure generated due to the relative motion between the contact surfaces leads to welding of asperities. As the sliding

continues, breaking of bonds generates micro cavities, which further cause tiny particles abrasion. Fig. 3a shows the wear traces micrographs of the 3 wt. % fine size SiC reinforced composites at higher load (49 N); wear traces clearly show the groove formation by the abrasive action of the asperities at the point of actual contact as presented in Figs. 3a. Fig. 3b shows the wear traces micrographs of the 3 wt. % coarse size SiC reinforced composites at higher load (49 N); the increased depth and width of the grooves indicate the transition from the mild wear to severe wear. The wear traces are also covered with the thin white oxide layer, which protects the matrix, but rupturing of the oxide layer leads to transition in the wear mode, [10], which is responsible for increase of the delamination area, as shown in Fig. 3b.

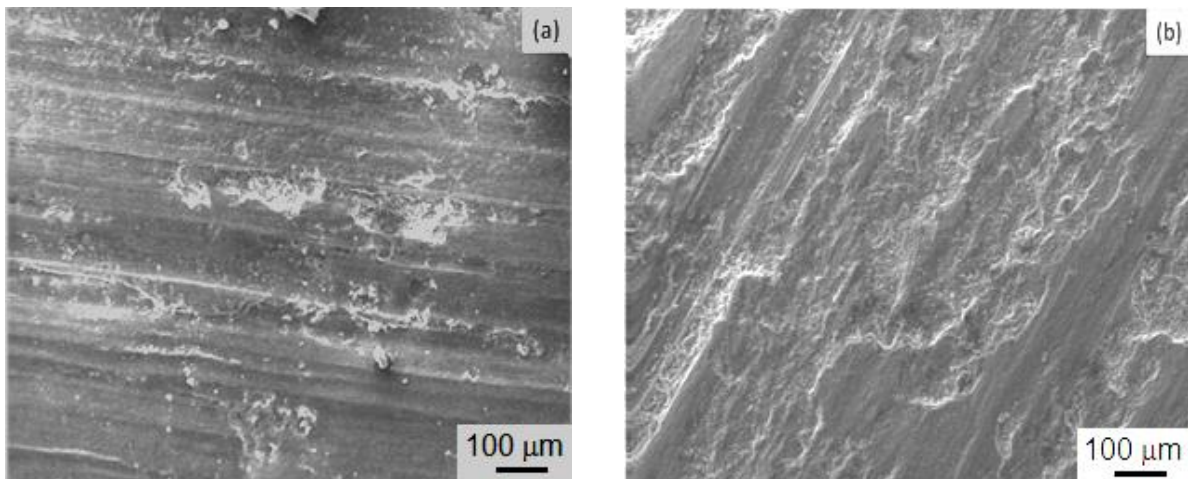
Fig. 4a shows the delaminated area along with the abrasive grooves on the worn surface of the 9 wt. % fine size SiC reinforced composite. Due to the presence of SiC particles in the matrix, abrasive grooves are created on the surfaces during the continuous sliding of the materials. Some adhesive debris is present on the wear trace due to the thermal welding between the contact areas, [11]. Surface presents the view of the delaminated area as observed in the micrograph (Fig. 4a). Fig. 4b shows the worn surface of the 9 wt. % coarse size SiC reinforced composite tested at 49 N. The larger delaminated area with deeper grooves indicates the higher wear rate due to the increased depth of the grooves because of the change in shape of asperities. The plastic deformation has left more patchy scars on the surface. At 49 N load, 9 wt. % coarse size SiC reinforced composite exhibits the worn surface with much more delaminated area and some sign of chipping out of particles during the wear test, which is responsible for the higher wear rate as shown in Fig. 4b.



a) fine size reinforced

b) coarse size reinforced

Fig. 3. The wear traces of composites at 49 N loads for 3 wt. %.



a) fine size reinforced

b) coarse size reinforced

Fig. 4. The wear traces of composites at 49 N loads for 9 wt. %.

4.3 Analysis of wear debris at applied peak loads

The size of debris of the 3 wt. % fine size SiC reinforced composite is smaller at higher load (49 N) as compared to 3 wt. % coarse size SiC reinforced composite. The flake type debris (Fig. 5a) gives the indication of adhesive wear due to the transfer of material from the contacting surfaces in relative motion due to the solid phase welding or localized bonding. Deep grooves along with the flake type structure formed under high stress can be easily seen on the debris in Fig. 5b, which indicates the high wear rate of the material. At the higher load (49 N) conditions, the wear loss is due to

the combination of adhesion and delamination. The delamination wear is prominent at higher load because of the fragmentation of oxide layer, which covers the surface due to the accelerated oxidation of the metal surface layers in contact, [12].

Fig. 6a shows that at higher load, (49 N), larger size debris (flake like shape is observed after the wear test and this type of wear debris indicates that the adhesive wear dominates in the sliding direction during the wear. Due to the adhesive nature at high load, metal is chipped out in the form of flakes as debris, however, the small size debris are generated by crushing of flakes at higher load, [13].

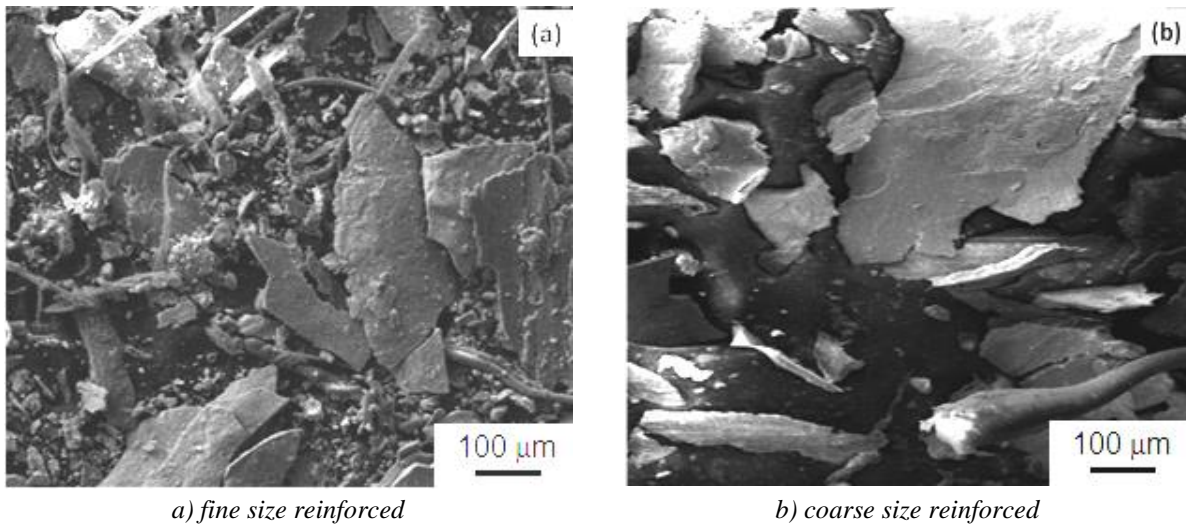


Fig. 5. The wear debris of composites at 49 N loads for 3 wt. %.

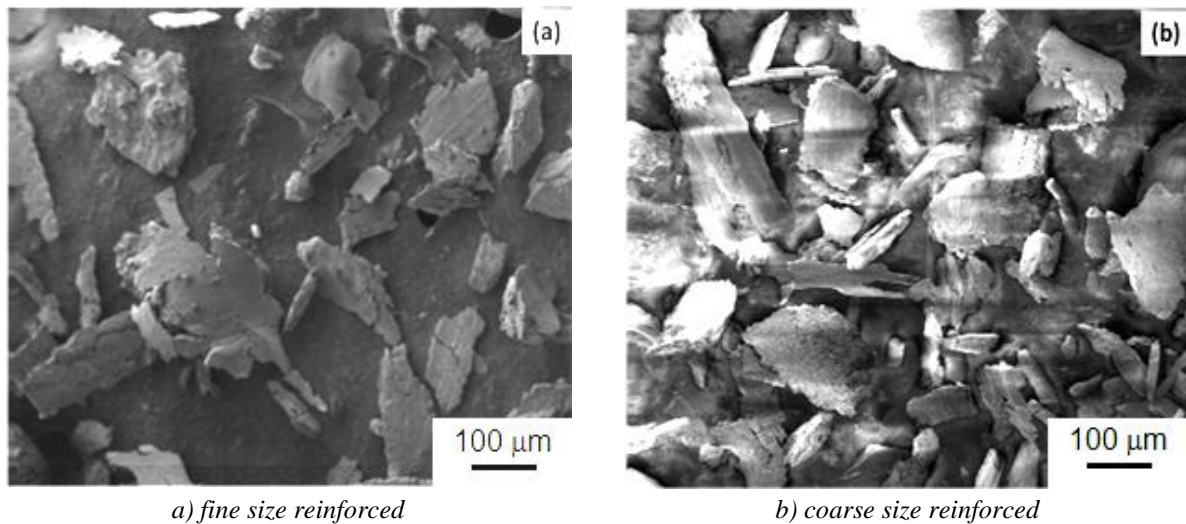


Fig. 6. The wear debris of composites at 49 N loads for 9 wt. %.

Some debris with grooves is observed in Fig. 6b, which indicates that the coarse particles have chipped out from matrix and those particles move between the contact surfaces in the sliding direction and generate grooves on the debris. Wear is governed by delamination, which gives plate-like morphology of debris with micro cracks, [8]. The large flat plate type morphology indicates the huge removal of material at higher load (49 N), which is shown in Fig. 6b. The fragmentation of debris was observed, which may be due to continuous rubbing of delaminated flakes between the contacting surfaces. The debris trapped in wear traces leads to a corrugated structure, shown in Fig. 6a.

5. Conclusion

In the present study, the particle reinforced metal matrix composite was developed by the stir casting process. To investigate the effect of SiC particles on the wear behavior of the composites, SiC particles of two sizes fine, and coarse were incorporated in two different amounts (3 and 9 wt. %). It was concluded from the study that at the higher loads more wear was noticed. From the experimental study was also observed that the wear resistance of the composite materials increases with an increase in reinforcement of SiC, although an increase the size of the reinforcement SiC does not result in an appreciable change of the wear rate.

The microstructural study of specimen after the wear test leads to the conclusion that both adhesive and abrasive wear mechanisms contribute for wear of composites.

Acknowledgement

The authors would like to thank Prof. Deepinder Singh, Head, Department of Mechanical Engineering, RIMT-IET, Mandi Gobindgarh, for his valuable suggestions for improvising this paper.

References

- [1] M. Singh, D.P. Mondal, O.P. Modi, A.K. Jha: *Wear* 253 (2002) 357-368.
- [2] S. Das, S. Das, K. Das: *Composite Science and Technology* 67 (2007) 746-751.
- [3] S. Das, V. Udarabanu, S. Das, K. Das: *J. Mater. Sci. Science* 41 (2006) 4668-4677.
- [4] R.L. Deuis, C. Subramaian, J.M. Yellup: *Composite Science and Technology* 57 (1997) 415-435.
- [5] N. Wang, Z. Wang, G.C. Weatherly: *Metall. Mater. Trans. A* 23 (1992) 1423-1431.
- [6] S.K. Chaudhury, A.K. Singh, C.S. Sivaramakrishnan, S.C. Panigrahi: *Wear* 258 (2005) 759-767.
- [7] A. Onat: *Journal of Alloys and Compounds* 489 (2010) 119-124.
- [8] G. Ranganath, S. C. Sharma, M. Krishna: *Wear* 251 (2001) 1408-1413.
- [9] S.A. Alidokht, A. Abdollah-zadeha, S. Soleymani, T. Saeid, H. Assadi: *Mater. Charact.* 63 (2012) 90-97.
- [10] Y. Mazaheri, M. Meratian, R. Emadi, A.R. Najarian: *Mater. Sci. Eng. A* 560 (2013) 278-287.
- [11] R. Yamanoglu, E. Karakulak, A. Zeren, M. Zeren: *Materials and Design* 49 (2013) 820-825.
- [12] S. Naher, D. Brabazon, L. Looney: *J. Mater. Process. Tech.* 143-144 (2003) 567-571.
- [13] M. Uthayakumar, S. Aravindan, K. Rajkumar: *Materials and Design* 47 (2013) 456-464.



MODELING OF AZ80 MAGNESIUM ALLOY CASTING PROCESS UNDER DIFFERENT ELECTROMAGNETIC FREQUENCY

Yuanyuan Bai¹, Rufei Wei^{2,3}, Qichi Le^{1*}, Haitao Zhang¹

¹ Key Laboratory of Electromagnetic Processing of Materials, Ministry of Education, Northeastern University, Shenyang, Liaoning 110004, China

² School of Metallurgy Engineering, Anhui University of Technology, Ma'anshan, Anhui 243002, China

³ Key Laboratory of Metallurgical Emission Reduction & Resources Recycling, Ministry of Education, Anhui University of Technology, Ma'anshan, Anhui 243002, China

*corresponding author: e-mail: qichil@mail.neu.edu.com (Q. Le), byy132@hotmail.com (Y. Bai)

Resume

The paper aims to clarify the effects of electromagnetic frequency on magnesium alloy AZ80 billets during low frequency electromagnetic casting. It proposes a mathematic model, verified against the temperature measurements obtained from AZ80 alloy billet of 160 mm in diameter, to predict the interaction of electromagnetic field, fluid flow, and temperature distribution. The sump depth becomes deeper and the maximum sustained speed of melt flow increases with the increase of electromagnetic frequency. By the analysis of the effects of fluid flow and temperature field on the solidification in the presence of electromagnetic field, the best electromagnetic parameters are given.

Article info

Article history:

Received 22 August 2016

Accepted 12 December 2016

Online 04 February 2017

Keywords:

Low frequency electromagnetic casting; Magnesium alloy; Temperature field; Fluid flow.

Available online: <http://fstroj.uniza.sk/journal-mi/PDF/2016/19-2016.pdf>

ISSN 1335-0803 (print version)

ISSN 1338-6174 (online version)

1. Introduction

Compared with steel and aluminum, magnesium (Mg) is used commonly as the lightest structural metal for the low specific gravity. Additionally, there are many other advantages of magnesium, such as high specific strength and specific stiffness, excellent damping capacity and recyclability, relatively good conductivity and shielding capacity, and etc. The magnesium alloy has a great potential to be used in automobile, electronic products, aerospace and defense. And the application of magnesium alloys grows at the fastest rate every year in the world [1 - 4]. The research of magnesium alloys has been more extensive since 2000. AZ80 alloy is one of the most typical cast Mg alloys with low price and good mechanical properties [5 - 8]. There have been several studies to investigate AZ80 magnesium alloy. Hilpert et al. [9] studied corrosion fatigue

behavior of the high-strength magnesium alloy AZ80 and showed that roller burnishing led to outstanding fatigue performance. In another study, effect of heat treatment on microstructure and tensile deformation of Mg AZ80 alloy at room temperature has been investigated. It has been shown that the dissolution of γ -phase in materials homogenized for 5 h significantly improves the casting's ductility [10]. Moreover, it has also been reported that continuous networks of β -Mg₁₇Al₁₂ formed along grain boundaries acted as effective crack propagation paths, which had negative effects on the weld strength [11].

Up to now, most of the magnesium alloy products are fabricated by direct chill (DC) casting. It is very easy to process foundry defects, especially hot cracking appearing in DC casting when filling of the mould cavity, because heat transfer, which takes place

between the metal surface and the walls of the mould, will directly affect the subsequent processing as genetic effect. Therefore, it is important to eliminate the casting defects in order to improve microstructure and properties of the alloy. Low-frequency electromagnetic casting (LFEC) is developed by Cui and his colleagues [12 - 15], which can improve properties of the alloy by precisely controlling the fluid flow and temperature field. Their research suggests the application of low-frequency electromagnetic field can refine microstructure of aluminum alloys remarkably, decrease the macro segregation, increase the mechanical properties of casting alloys, and improve the surface quality of ingot and hinder crack efficiently.

In addition, with the development of finite element calculation, numerical simulation has become the effective and convenient technology tools of engineering analysis science research besides experiment and theory. A large number of experiments were performed to obtain best process parameters, but this resulted in costly and time consuming and sometimes it was impossible in the past. Thus, the process was modeled and analyzed by the finite element method at first, and then the result was verified by experiments. Many mathematical models for a continuous casting process have been developed. There are also some studies about semi-continuous casting process simulation when the low-frequency electromagnetic exists. Zhang et al. [16, 17] presented a numerical simulation model for 7XXX aluminum alloys which could predict electromagnetic field, fluid flow, heat transfer and solidification during low frequency electromagnetic casting. Yoshioka et al. [18] studied the heat transfer and solidification processes of alloy melt with undercooling. In this investigation, an analytical model was proposed to predict the temperature change, interface movement, and solute concentration distribution during the solidification of an undercooled Bi-Sn melt. Faraji et al. [19]

investigated the finite element method (FEM) and an experiment of the accumulative back extrusion (ABE) processing of an AZ91 magnesium alloy. Le et al. [20] studied the effect of electromagnetic field on the hot-top casting by numerical simulation. Kageyama et al. [21] developed a three dimensional numerical model and predicted the behavior of steel in the field of an electromagnetic caster. Bermudez et al. [22] studied the ingot temperature in DC and EMC metal castings, and they solved the free boundary problem using a fixed domain method. Shao et al. [23] investigated the influence of low frequency electromagnetic field and power ultrasonic field on DC casting. However, there are few reports that discuss the effects of low-frequency electromagnetic field on AZ80 magnesium alloy systematically during DC casting with the mold of forged aluminum by numerical calculation.

In this paper, the FEM and an experimental investigation were performed to investigate the effects of the electromagnetic field on the semi continuous casting of AZ80 magnesium alloy. This developed model includes non-linear material properties of specific heat and thermal conductivity as well as phase changes during solidification.

2. Numerical simulations

Many facts influenced the flow and heat transfer of melt, in order to solve the problem, the model were simplified and some necessary assumptions were given:

- (1) The meniscus shape and calculation of the solute field were not comprised in the study.
- (2) The molten magnesium alloys deemed as an incompressible fluid, so the density of the melt was set down as constant.
- (3) The effect of displacement current was ignored. Because the molten metal is good conductor of electricity in which the charge relaxation time is much lower than the transit time of electromagnetic waves.

(4) The distribution of the magnetic field was not influenced by the variety of the fluid field. As for LFEC process of magnesium alloys, the magnetic Reynolds number R_m is less than 1 (where μ is permeability, σ the electric conductivity, U_0 the characteristic velocity and L_0 is characteristic length), which will result the second term of right hand side of the Ohm's Law ($J=\sigma(E+U\times B)$) is ignored.

(5) Joule heating was not considered in this model because it was so tiny compared with the total quantity of heat in the system. Compared to the entropy inflow with the liquid magnesium, the Joule heat produced during LFEC process is so small that can be ignored.

The governing equations in calculation of LFEC process are expressed as follows [17]:
Ampere's law:

$$\nabla \times E = -\frac{\partial B}{\partial t} \quad (1)$$

Faraday's law:

$$\nabla \times B = \sigma E \quad (2)$$

Gauss's law of electric field:

$$\nabla \cdot E = 0 \quad (3)$$

Gauss's law of magnetic field:

$$\nabla \cdot B = 0 \quad (4)$$

where E is the electric field intensity vector, B is the magnetic flux density vector; t is the time and σ the electric conductivity.

It is essential to give a constitutive equation about electromagnetic volume density f_{em} , which can be given as:

$$f_{em} = J \times B \quad (5)$$

On the basis of hypothesis (4), the conduction current J can be expressed as:

$$J = \sigma E \quad (6)$$

The time average electromagnetic volume force density F which is introduced to link electromagnetic field and other physics fields can be obtained as:

$$F = \frac{1}{2} R_e (J \times B) \quad (7)$$

where, R_e is the real part of a complex quantity.

Computer simulations of the effects of various casting conditions on the steady-state temperature distribution and sump profile and flow patterns during LFEC process of AZ80 alloy are performed with ANSYS software. To analyze the problem, 2-Dimensional models are constructed in ANSYS finite element software. Considering the symmetry, only one half of the billet is modeled. The calculation domain 1600 mm high and 80 mm in radius is divided into rectangular blocks. Thermophysical parameters used in these simulations are described in Fig. 1. The boundary conditions at the inlet and outlet are a constant temperature and a constant velocity. All free surfaces are treated as the static adiabatic wall. Symmetry axis boundary condition is applied to axisymmetric boundary condition. Mold cooling refers to the region where the billet is within the mold at a given time. Equation (8) and (9) expresses these boundary conditions:

$$k_{thermal} \frac{\partial T}{\partial n} = h(T - T_{en}) \quad (8)$$

$$h = h_{contact}(1 - f_s) + h_{air} \times f_s \quad (9)$$

where h is the heat transfer coefficient at the boundary; T_{en} is the environment temperature and it is set to 323 K; $h_{contact}$ is the heat transfer coefficient at the mold and is given as 1000 W m⁻²K⁻¹; h_{air} is the heat

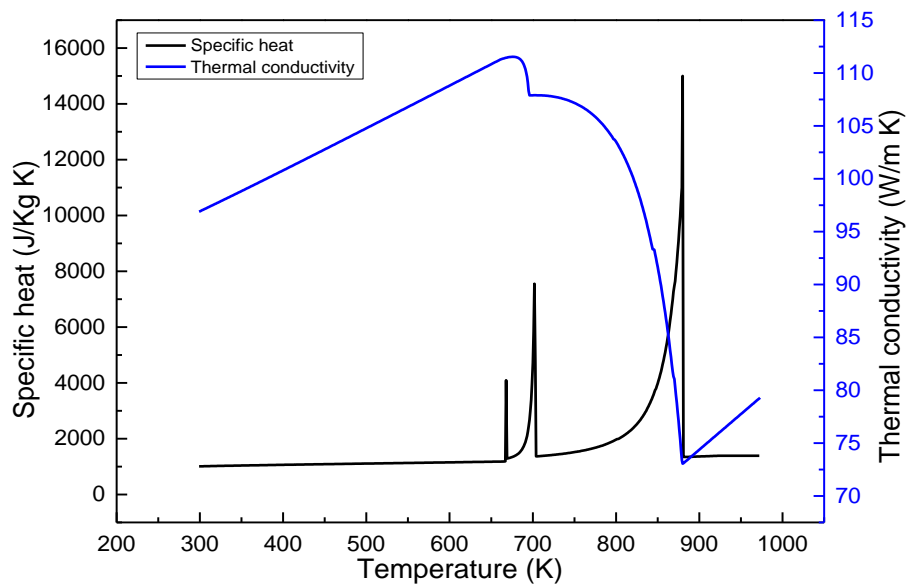


Fig. 1. The values of specific heat and thermal conductivity.
(full colour version available online)

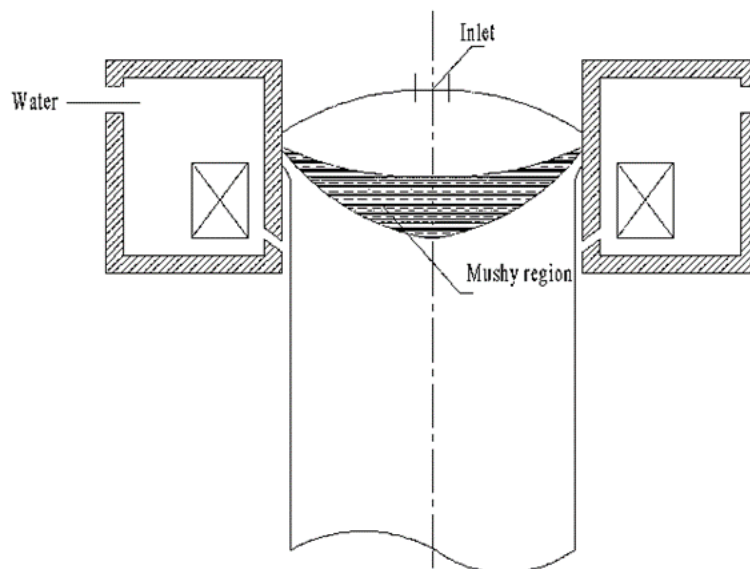


Fig. 2. Schematic diagram of LFEC process of AZ80 Mg alloy billets

is comprised of two regions: the impingement zone and the free falling zone, which refer to the areas below the mold that are in contact with water. The idealized boiling water curves describe the relationships to the heat transfer coefficient during secondary cooling [24]. This boundary condition is treated as the moving wall, and its velocity is $0.00133 \text{ m}\cdot\text{s}^{-1}$. In addition, the environment temperature is given as 300 K. Calculations

are stopped as soon as the steady state is achieved.

3. Experimental procedures

The material used in this study was an as-cast AZ80 magnesium alloy with a main composition of Al 7.9 – 9.2, Zn 0.7 – 0.8, Mn 0.12 – 0.15, and Mg balance. High purity Mg, Al, and Zn were used to prepare the alloys, Mn was added in the form of Al-9 wt. % Mn

master alloy, respectively. The melting experiment of alloy was conducted by a self-developed resistance furnace under the No. 2 covering flux and $\text{CO}_2 + 0.5 \text{ vol. \% SF}_6$ atmosphere, which was to protect molten magnesium from oxidation (Fig. 2).

Since the liquidus temperature of the alloy was 880 K, the melt was overheated to $930 \pm 5 \text{ K}$; this temperature had been verified to maintain the alloy composition as its initial ingredient. The metal was held for 20 min to ensure the alloying elements were completely dissolved and a homogenous composition was obtained. The melt was poured to a water-cooled mold with a diameter of 160 mm, a height of 120 mm and a wall-thickness of 10 mm at 930 K and cast into billets with a diameter of 160 mm at a velocity of $0.00133 \text{ m}\cdot\text{s}^{-1}$. The cooling water flow rate was $70 \text{ L}\cdot\text{min}^{-1}$ during the casting. The electromagnetic field was applied by a 100 turns water-cooling copper coil surrounding the mold made of forged aluminum. The experiment of LFEC results was compared with the simulation results. The cooling curves

of different positions of the LFEC ingots were measured by means of five K-type chromel-alumel thermocouple, which were even distribution of radial direction of billet.

4. Results and discussions

4.1 Comparison between calculated results and experimental results

Fig. 3 shows the comparison of between the calculated results and the measured results for cooling curves at distance of 0, 0.04 and 0.08 m from the center of the billets during the LFEC process. It is found that numerical simulation results are basically consistent with the experiment results and the model is effective and feasible. First, the temperature of melt slow descends to liquidus due to the conduction of the mould and cooling water, and then the temperature continues to decrease at a higher rate but the cooling rate of measured positions are totally different. Additionally, the cooling rate in the edge position of billet is significant higher than other position because there is a larger thermal conductivity rate at the region closed to the mould.

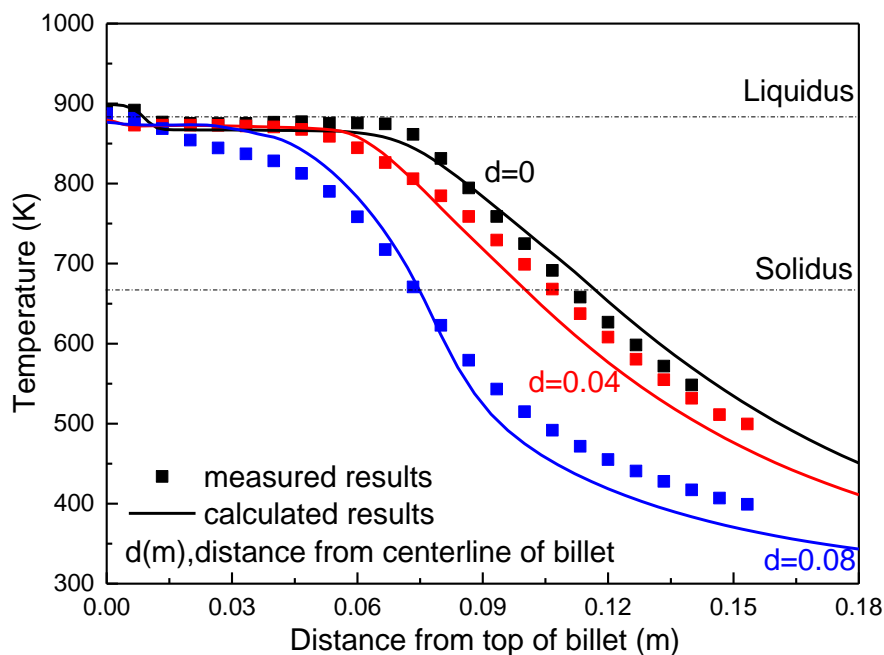


Fig. 3. Comparison between the calculated and measured results: the cooling curves in LFEC processing. (full colour version available online)

In order to investigate the effects of electromagnetic parameters on distribution of temperature field, fluid flow and heat transfer, all parameters except electromagnetic frequency and intensity are fixed. In the first place the effect of frequency is mainly analyzed, therefore, the

electromagnetic intensity keeps being 6000At, and electromagnetic frequency is set as 10 Hz, 20 Hz, 30 Hz, 50 Hz and 100 Hz, respectively. In the second place, the electromagnetic frequency keeps being 30 Hz, and electromagnetic intensity is set as 6000 At, 9000 At, 12000 At, respectively.

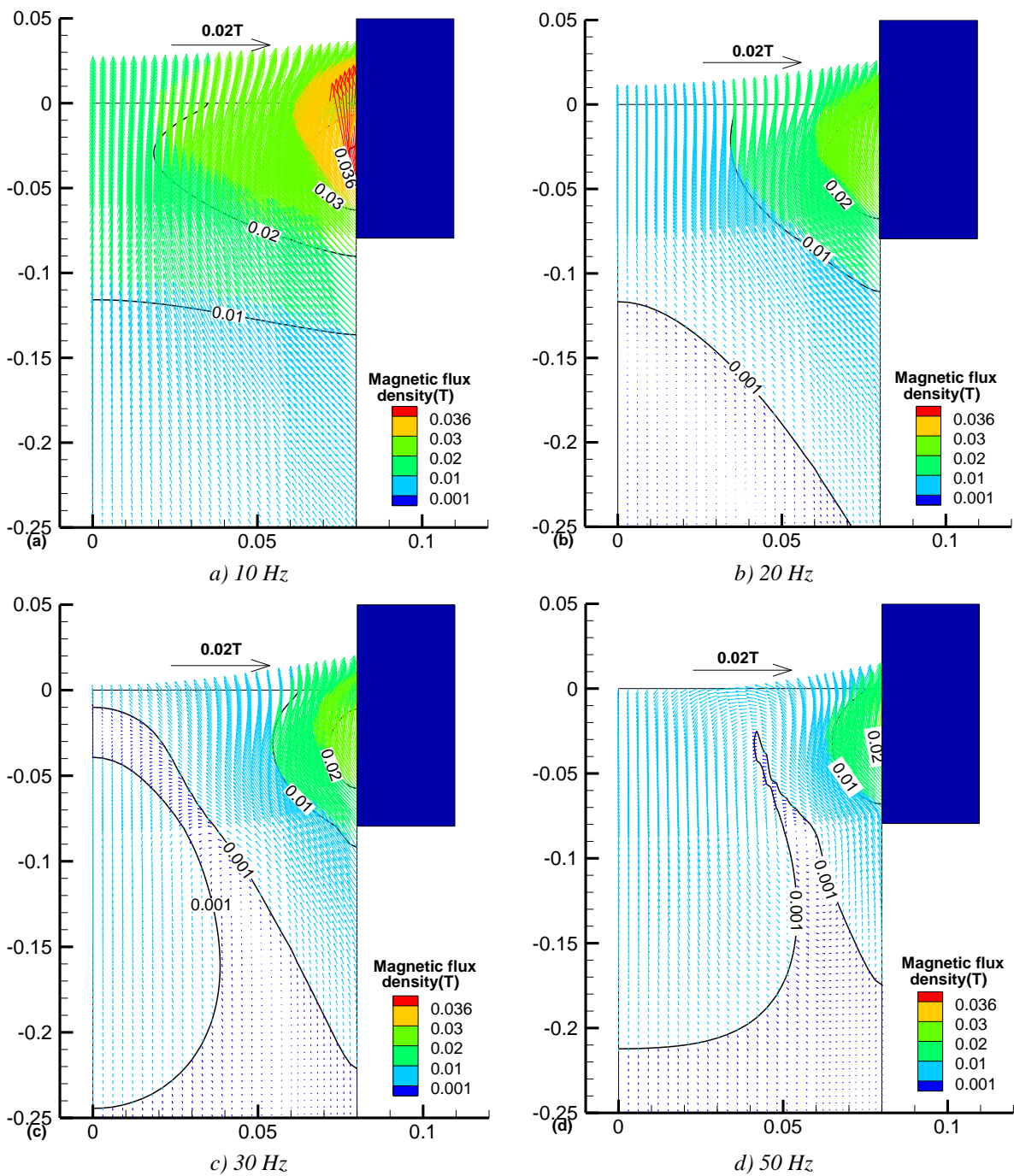


Fig.4. Magnetic flux density contours and vectors under different electromagnetic frequency.
(full colour version available online)

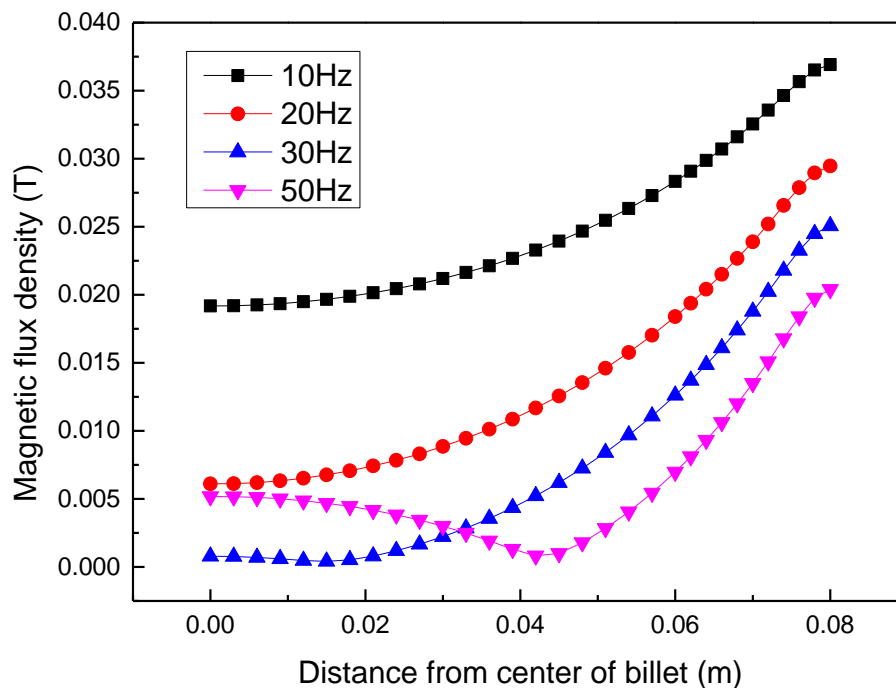


Fig.5. Magnetic flux density from the surface to the center of the billets on the given path ($y = -0.035$ in Fig.4) under different electromagnetic frequency.

(full colour version available online)

4.2 Magnetic flux density

The magnetic flux density contours and vectors in the billets cast during the LFEC process at various electromagnetic frequency are shown in Fig. 4. It is found that the maximum of magnetic flux density decrease slowly with the increase of electromagnetic frequency. Due to the skin effect of alternative electromagnetic field, the magnetic flux density declines from the surface to the center of billet, when the frequency is lower level (10 Hz and 20 Hz). Additionally, there is a vortex of magnetic flux density in the billets when the frequency is over 30 Hz. Fig. 5 shows variation of magnetic flux density on given path ($y = -0.035$ in Fig. 4) from the center of billets to the outer surface of the mold under different electromagnetic frequency. The distribution of electromagnetic wave in conductor can be expressed as equation (10):

$$B = B_0 e^{-r\sqrt{\pi f \mu \sigma}} \quad (10)$$

where r is the distance from the surface to the center of billets along the given path, f the frequency and B_0 is the magnetic flux density at the surface of billets along the given path. From this we could know the magnetic flux density decreases exponentially from surface to the center of billet, and the attenuation rate increases with increasing frequency. Nevertheless, the magnetic flux density decreases first and then increases when the frequency exceed 30 Hz, and there is a trend to the surface of billet on the location of the minimum of the magnetic flux density as seen in Fig. 5. The main reason is that the eddy current introduced by the source current in the coil, which is opposite to the source current. The electromagnetic field of same frequency generated by the eddy current also is opposite to the electromagnetic field generated by the source current. The magnetic flux density showed in Fig. 4 is the superimposed result of the two electromagnetic fields mentioned above. The penetrating depth of electromagnetic field

produced by the source current is larger than the eddy current when the frequency is low. Therefore, the magnetic flux density attenuates exponentially from surface to the center of billet under frequency of 10 Hz, 20 Hz and 30 Hz. However, the penetrating depth electromagnetic

field produced by the source current is shallower than that by the eddy current in the center zone of billets when the frequency is greater than 30 Hz, which results in the varying of magnetic flux density in the center of billets.

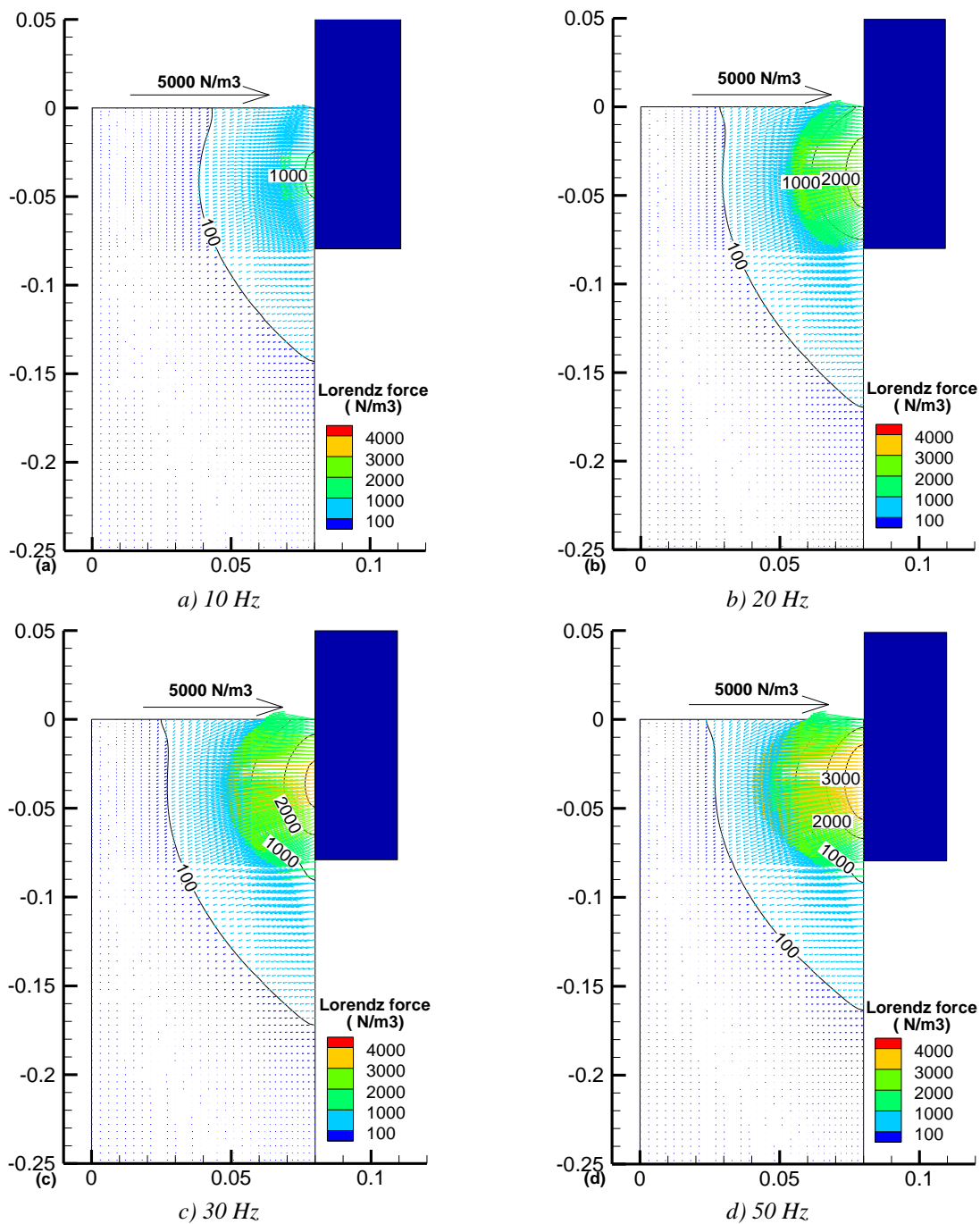


Fig.6. Time average electromagnetic volume force density contours and vectors under different electromagnetic frequency.
(full colour version available online)

4.3 Time average electromagnetic volume force density

Fig. 6 shows the time average electromagnetic volume force density contours and vectors when electromagnetic frequency is in the range of 10 – 50 Hz. It is found that the time average electromagnetic volume force density in the area of skin effect increases when electromagnetic frequency increase. In addition, the increase of frequency has no effect on the direction of the electromagnetic volume force density. The time average electromagnetic volume force from the surface to the center of the billets on the given path ($y = -0.035$ in Fig. 4) under different electromagnetic frequency are shown in Fig. 7. The direction of the electromagnetic volume force density on the path is perpendicular to the surface and pointing to the center of billets. According to reference [16],

$$F = F_0 e^{-2r\sqrt{\pi f \mu \sigma}} \quad (11)$$

where F_0 is the electromagnetic volume force

density at the surface of billets along the given path. In the light of Eq. (11), like the magnetic flux density, the electromagnetic volume force density decreases exponentially from surface to the center of billet, and the attenuation rate increases with increasing frequency, as seen in Fig. 7.

4.4 Fluid flow field

Figs. 8 - 10 show velocity vectors, velocity profiles and streamline patterns under different electromagnetic frequency. The melt flow is similar for all four different cases. The direction of melt flow is not changed with electromagnetic frequency as seen in Fig. 8. It is, however, clearly seen that the maximum velocity of melt flow increases with increasing electromagnetic frequency in Fig. 9, which is same with the change trend of electromagnetic volume force. In addition, it is observed that there is a larger eddy current in molten pool and a small circulation near the solidification front at the surface region of the billet from Fig. 9. Moreover the location of maximum velocity is near the surface of billet, and the location of minimum velocity

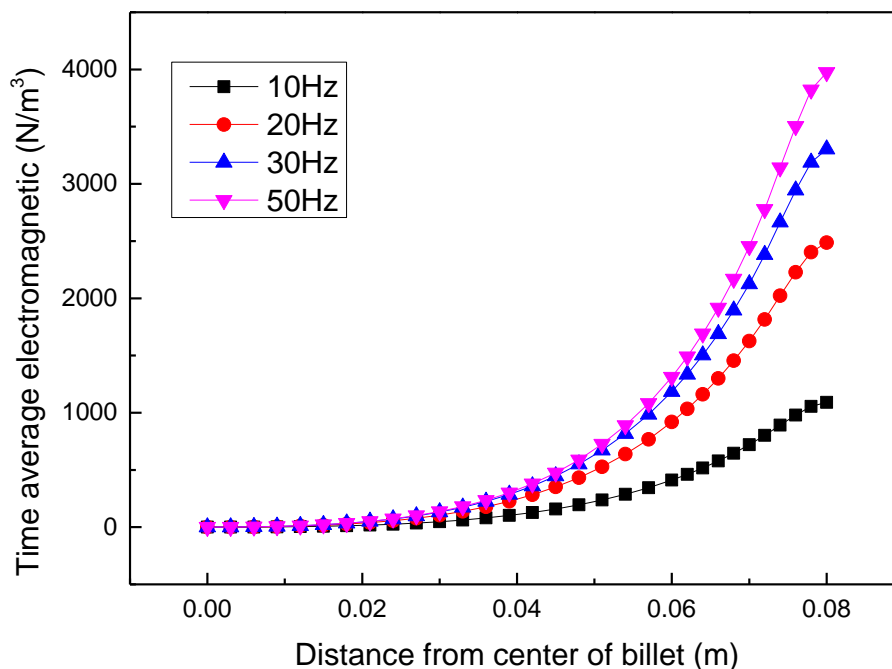


Fig.7. Time average electromagnetic volume force from the surface to the center of the billets on the given path ($y = -0.035$ in Fig.4) under different electromagnetic frequency. (full colour version available online)

is the inlet. The location of maximum velocity moves to the center of billet with the increase of electromagnetic frequency. The velocity distribution is non-uniform in the given path when the electromagnetic frequency is 10 Hz. As shown in Fig. 11, the velocity is quite well-distributed when electromagnetic frequency is in the range of 20 – 50 Hz.

It is reason that zone of electromagnetic force reduces when electromagnetic frequency increases, caused by the electromagnetic penetration depth decreases with the increase of electromagnetic frequency. It means that the non-evenness of flow due to the skin effect of alternative electromagnetic field.

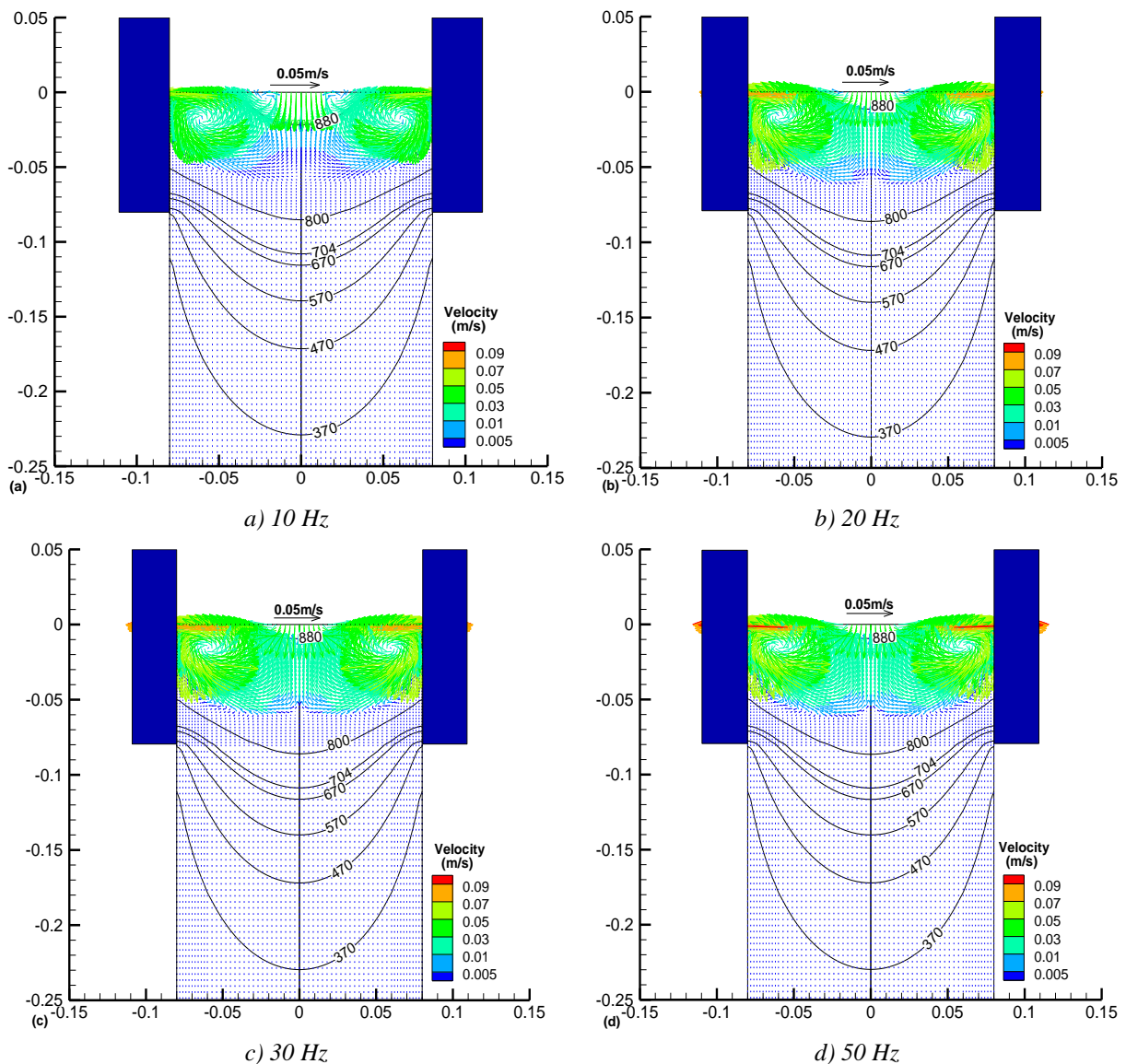


Fig.8. Velocity vectors with temperature profiles under different electromagnetic frequency.
(full colour version available online)

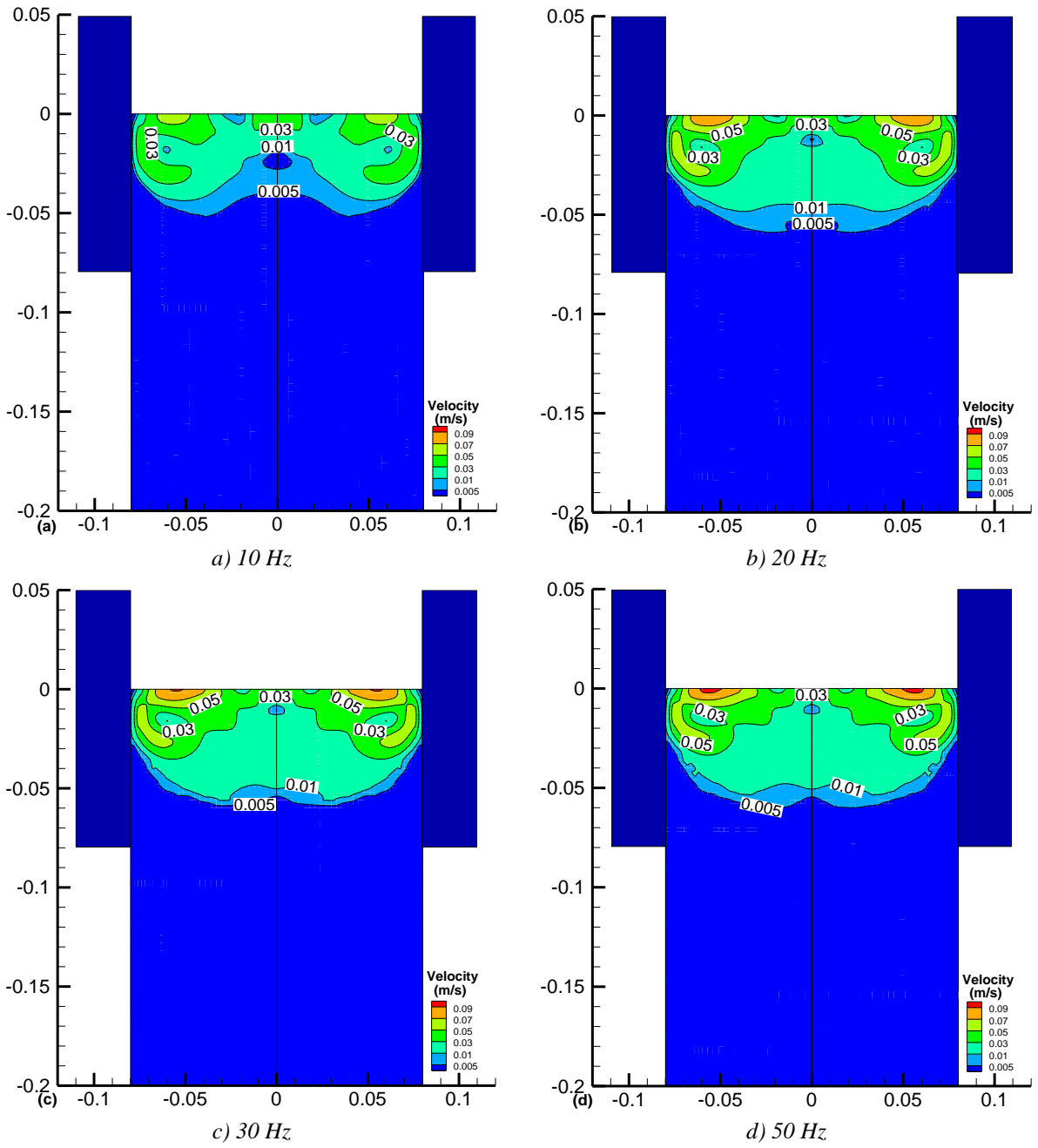


Fig.9. Velocity profiles under different electromagnetic frequency.
(full colour version available online)

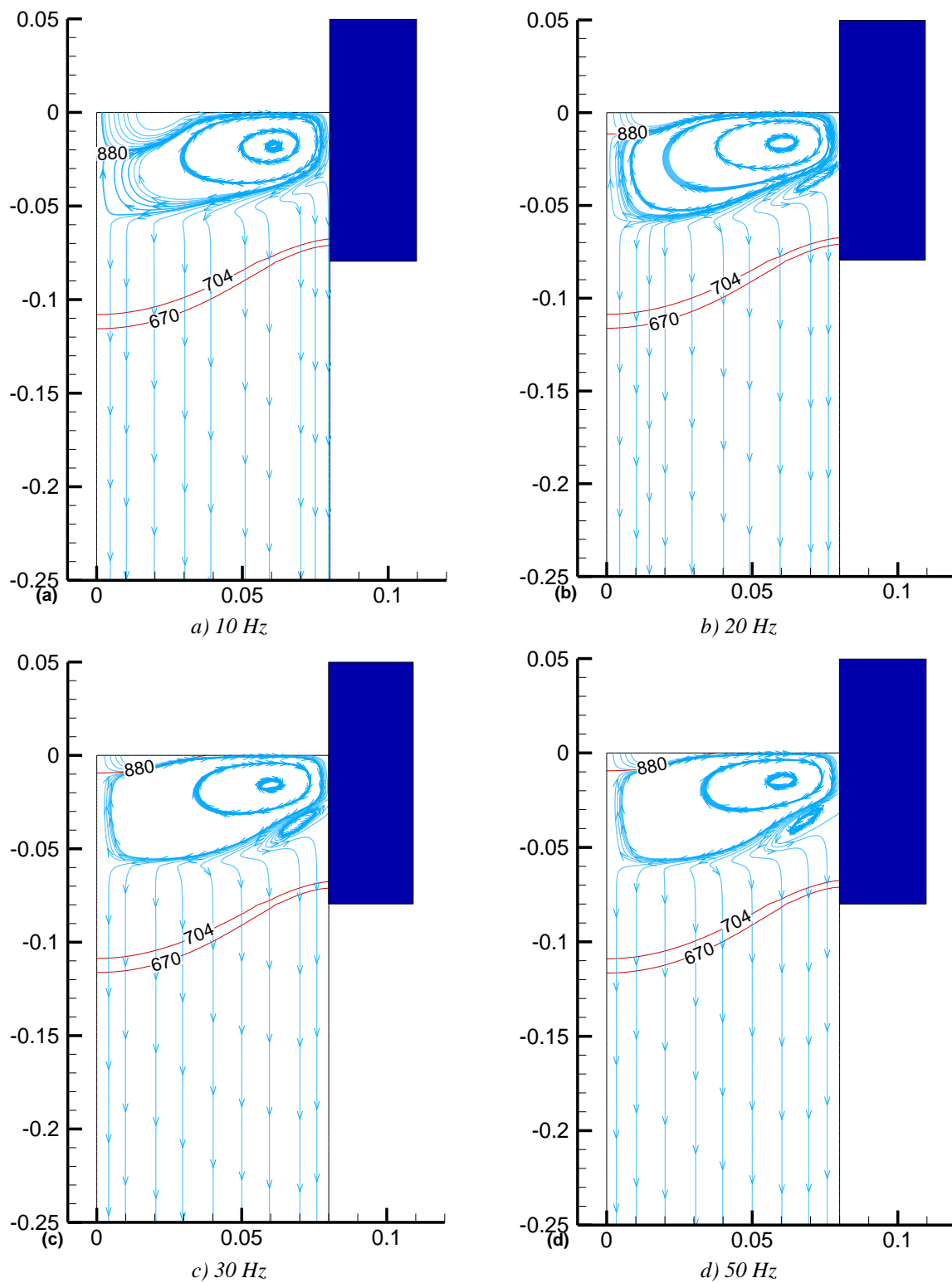


Fig.10. Streamline patterns with temperature profiles under different electromagnetic frequency.
(full colour version available online)

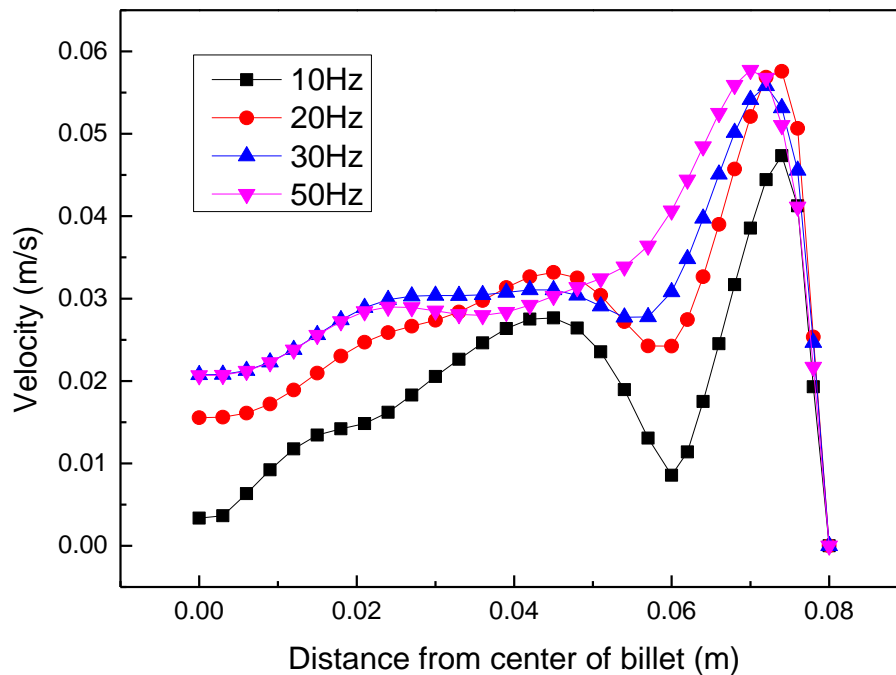


Fig.11. Velocity on the given path ($y=-0.02$ in Fig.4) under different electromagnetic frequency. (full colour version available online)

4.5 Temperature field

The temperature profiles under different electromagnetic frequency are shown in Fig. 12. It is found that the uniform temperature distribution is obtained under the function of electromagnetic field. However, the temperature field is influenced little by the electromagnetic frequency. Fig. 13 shows the sump shape and sump depth under different electromagnetic frequency. It is observed that electromagnetic frequency has no effect on the sump shape, and the sump depth becomes deeper with the increase of electromagnetic frequency, but it shows a little drop as the frequency is 30 Hz. This is because the increase of intensity determined by the electromagnetic volume force.

5. Conclusions

In this study, the effects of electromagnetic frequency on AZ80 alloys during DC casting process are investigated. The study has focused on the influence of electromagnetic field on the magnetic flux density, time average electromagnetic volume force density, flow field and temperature field. The model could be used to predict the optimum process parameters on electromagnetic frequency and electromagnetic intensity.

Increasing the electromagnetic frequency leads to a decrease in magnetic flux density, an increase in electromagnetic force, first rise and then descending in relative velocity, and tiny changes in temperature field. The uniform temperature field can be obtained by electromagnetic frequency more than 30 Hz.

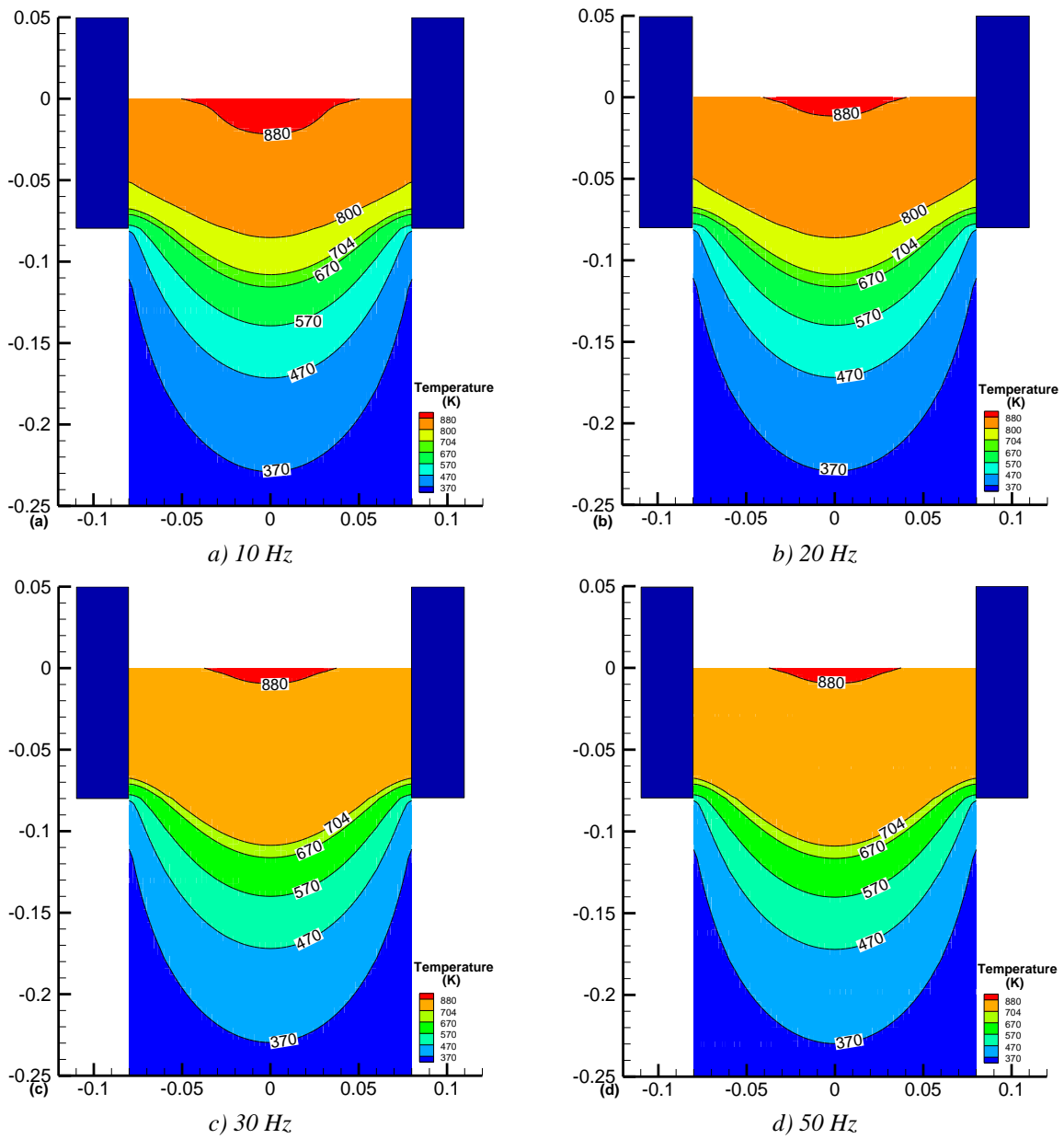
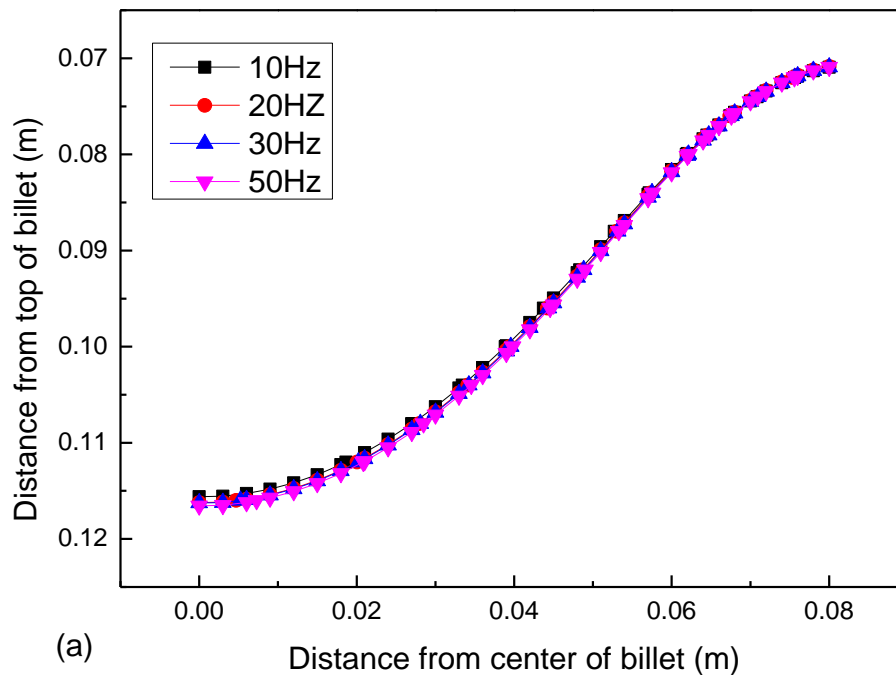
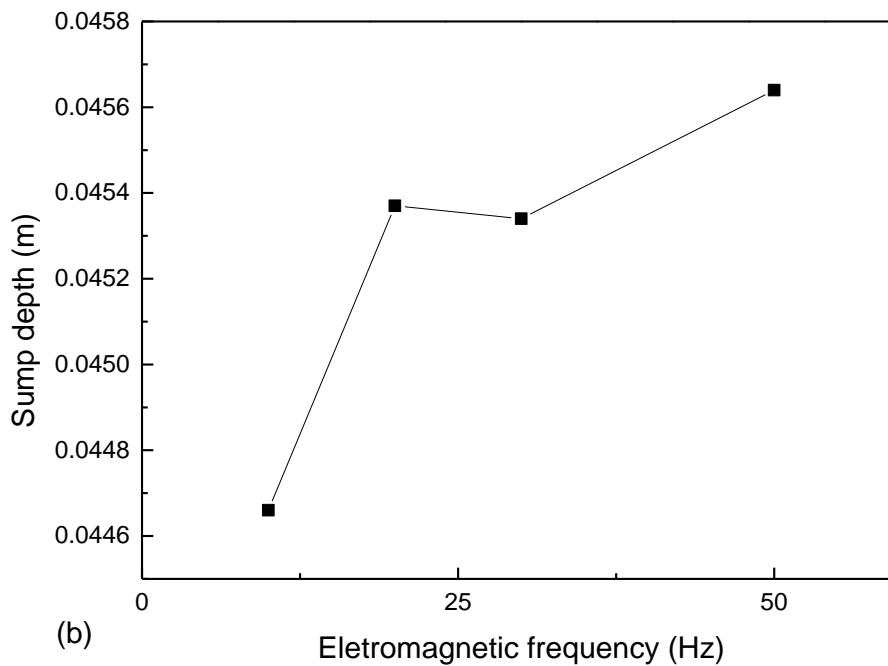


Fig.12. Temperature profiles under different electromagnetic frequency.
(full colour version available online)



a) on sump shape



b) on sump depth

Fig. 13. The effect of electromagnetic frequency.

(full colour version available online)

Acknowledgement

This research was financially supported by the Major State Basic Research Development Program of China (Grant No. 2013CB632203), the National Basic Research Program of China (Grant number 2012CB723307-03) and the National Key Research and Development

Program of China (Grant No. 2016YFB0301104)

References

- [1] F. Fereshteh-Saniee, K. Fallah-Nejad, A. S. Beheshtiha, H. Badnava : Materials and Design 50 (2013) 702-712.

- [2] M. Li, T. Tamura, K. Miwa: *Acta Materialia* 55(14) (2007) 4635-4643.
- [3] B. L. Mordike, T. Ebert: *Mater. Sci. Eng. A* 302(1) (2001) 37-45.
- [4] W. Xiao, M. A. Easton, S. Zhu, M.S. Dargusch, M. A. Gibson, S. Jia, J. Nie: *Adv. Eng. Mater.* 14(1-2) (2012) 68-76.
- [5] S. Barbagallo, H. Laukli, O. Lohne, E. Cerri: *J. Alloys Compd.* 378(1) (2004) 226-232.
- [6] Y. Uematsu, K. Tokaji, M. Kamakura, K. Uchida, H. Shibata, N. Bekku: *Mater. Sci. Eng. A* 434(1) (2006) 131-140.
- [7] Z. Wang, Y. Yang, B. Li, Y. Zhang, Z. Zhang: *Mater. Sci. Eng. A* 582 (2013) 36-40.
- [8] N. Kashefi and R. Mahmudi: *Materials & Design* 39 (2012) 200-210.
- [9] M. Hilpert, L. Wagner: *J. Mat. Eng. Perform.* 9(4) (2000) 402-407.
- [10] I. Yakubtsov, B. Diak, C. Sager, B. Bhattacharya, W. MacDonald, M. Niewczas: *Mater. Sci. Eng. A* 496(1) (2008) 247-255.
- [11] S. T. Niknejad, L. Liu, T. Nguyen, M.-Y. Lee, S. Esmaeili, N.Y. Zhou: *Metallurgical and Materials Transactions A* (2013) 1-10.
- [12] J. Dong, Z. Zhao, J. Cui, F. Yu, C. Ban, *Metallurgical and Materials Transactions A* 35(8) (2007) 2487-2494.
- [13] B. Zhang, J. Cui, G. Lu: *Materials Letters* 57(11) (2003) 1707-1711.
- [14] B. Zhang, J. Cui, and G. Lu: *Mater. Sci. Eng. A* 355(1) (2003) 325-330.
- [15] Y. Zuo, J. Cui, Z. Zhao, H. Zhang, L. Li, Q. Zhu: *J. Mater. Sci.* 47(14) (2012) 5501-5508.
- [16] H. Zhang, H. Nagaumi, and J. Cui: *Mater. Sci. Eng. A* 448(1-2) (2007) 177-188.
- [17] H. Zhang, H. Nagaumi, Y. Zuo, and J. Cui: *Mater. Sci. Eng. A* 448(1-2) (2007) 189-203.
- [18] H. Yoshioka, Y. Tada, K. Kunimine, T. Furuichi, and Y. Hayashi: *Acta Materialia* 54(3) (2006) 765-771.
- [19] M. Mohamadzadeh, A. Rostampour Haftkhani, G. Ebrahimi, and H. Yoshihara: *Materials & Design* 35 (2012) 404-413.
- [20] Q.-C. Le, S.-J. Guo, Z.-H. Zhao, J.-Z. Cui, X.-J. Zhang: *J. Mater. Process. Tech.* 183(2-3) (2007) 194-201.
- [21] R. Kageyama: *Isij International* 42(2) (2002) 163-170.
- [22] A. Bermúdez, M. Otero: *Finite Elem. Anal. Des.* 40(13) (2004) 1885-1906.
- [23] Z. Shao, Q. Le, Z. Zhang, J. Cui: *Materials & Design* 32(8-9) (2011) 4216-4224.
- [24] H. Hao, D. Maijer, M. Wells, S. Cockcroft, D. Sediako, S. Hibbins: *Metallurgical and Materials Transactions A* 35(12) (2004) 3843-3854.